Emulation of Anyonic Statistics using High-Fidelity NMR Quantum Information Processing (QIP) Techniques

by

Jihyun Annie Park

A thesis
presented to the University of Waterloo
in fulfillment of the
thesis requirement for the degree of
Master of Science
in
Physics-Quantum Information

Waterloo, Ontario, Canada, 2015

I hereby declare that I am the sole author of this thesis. This is a true copy of the thesis, including any required final revisions, as accepted by my examiners.

I understand that my thesis may be made electronically available to the public.

Abstract

NMR control techniques have made many important contributions in developing set of tools for optimal quantum control, ranging from spin echo to dynamical decoupling. Using such optimal quantum control techniques, the emulation of what are known as anyonic statistics was demonstrated previously [5]. This demonstration showed the ability of NMR QIP for experimental exploration of topological quantum computing where anyonic statistics play a significant role as a means to implement the quantum gates by braiding anyons. In this thesis, going one step further than the previous demonstration, we experimentally emulated the anyonic statistics and demonstrated the path independence of anyonic braiding operations manifested in a 7-qubit Kitaev's lattice model[15]. In our experiments, the anyons are braided along two different loops in which the system's wave function gains a π phase in theory. We experimentally measured the anyonic phases of $(153.9 \pm 3.8)^\circ$ and $(151.4 \pm 3.8)^\circ$ for the two different braiding paths, demonstrating that experimental anyonic phases are path independent. However, the values differ from the theoretical value due to decoherence and gate imperfections.

Acknowledgements

First of all, I would like to thank my supervisor, Dr. Raymond Laflamme. After learning about quantum mechanics for the first time in my third year of undergraduate years, I could not resist but to learn more about quantum physics. However, as most of my undergraduate education has been geared towards biophysics/ medical physics, it was challenging for me to find a place in quantum research as a graduate student. Therefore, I truly appreciate the opportunity that Dr. Laflamme provided me which allowed me to step into quantum research for the first time. Moreover, I also thank him for introducing me to the interesting research topic. Through this project, I found my passion for experimental physics. Especially, I enjoyed observing beautiful peaks in NMR spectra. Therefore, I thank Dr. Laflamme for introducing me to NMR QIP.

Secondly, I would like to thank Dawei Lu and Emma McKay. It was a great experience to work on the project together with them, and I learned a lot from both. Dawei taught me how to use the spectrometer and nuts and bolts of NMR QIP. I was impressed by how quickly he understands my questions, and he had answers or guidances to my problems all the time. His immense knowledge and willingness to teach me inspired me work harder. Emma joined the team towards the end of my master's program, and with her contribution to the project, we were able to get the best experimental results. It was a great experience to share these moments with her. Also, I thank her proof-reading every single page of my thesis and providing me critical suggestions. This whole process would not have been possible without her.

I also want to give a special thank to Hemant Katiyar. Although he was not directed involved in the project, he provided many insightful suggesions. He would not hesitate to spend hours and hours on discussion. These experiences truly accelerated my learning.

I would also like to thank Sumit Sijher, Aharon Brodutch, Nayeli Azucena Rodriguez Briones, Daniel Park, Yuval Sanders and Chris Chamberland for helpful discussions and guidances throughout my master's program.

Lastly, I thank Dr. Matteo Mariantoni, Dr. Robert Knig, and Dr. Jonathan Baugh for agreeing to be on the committee.

Dedication

I would like to dedicate this thesis to Park family,

Kyu-Cheol Park
Mi-kyoung Lee
Ji-hee Park
Joon-hyeok Park

Table of Contents

List of Tables

Chapter 1

Motivation and Objectives

Ever since the first observation of nuclear magnetic resonance (NMR) in the late 1930s, NMR has been one of the most powerful tools used not only in research areas for tasks such as characterizing molecular structures and determining purity of chemical compounds, but also in ordinary medical applications [31, 4]. Starting from the late 90s, NMR techniques also became essential for quantum information processing (QIP), a field of manipulating quantum mechanical properties to process information. In the late 90s, there were already sophisticated NMR techniques available to characterize an internal Hamiltonian of a few qubit molecules [4]. Therefore, much of the dedication of NMR QIP has been geared towards developing experimental control techniques to precisely manipulate nuclear spins. Such developments enhanced our understanding of controlling not only nuclear spins, but also other quantum systems in general. The optimal quantum control using NMR QIP explores areas such as reducing the impact of unwanted system-environment interactions (dynamical decoupling such as Hahn Echo [10, 21, 37, 42], RF selection [34]), advances in pulse engineering (composite pulses [22], strongly modulated pulses [7], Gradient Ascent Pulse Engineering (GRAPE) [14]), and refocusing unwanted internal interactions (pulse compiler [34]). Therefore, NMR QIP has been a practical test-bed to experimentally demonstrate theoretical QIP ideas in the laboratory. In this thesis, using some of the control techniques developed, we experimentally emulate anyonic statistics manifested in Kitaev's Lattice Model using NMR QIP to explore the ideas of topological quantum computing, a quantum computational model based on braiding quasi-particle anyons.

Anyonic statistics play an important role in topological quantum computing (TQC) as a method to implement robust quantum gate by braiding the quasi-particle anyons. One of the reasons why such a braiding operation is resilient to noise is related to its path independent property. Due to the path independent property, it is not necessary to braid anyons following the exact path

but rather there can be wiggles in the path, providing flexibility to experimentalists. By emulating such statistics manifested in the 7-qubit Kitaev's lattice model, we answer the following questions:

- Are the braiding operations in the 7-qubit model resilient to decoherence of our experimental system?
- Can we experimentally demonstrate the path independence property of anyonic braiding using NMR QIP?

In chapter 2, I introduce what anyons are, the basic concepts of topological quantum computing using anyons, and how some of the key anyonic properties in TQC are manifested in Kitaev's lattice model. Closing chapter 2, the 7-qubit model for our experimental proposal is briefly discussed.

In chapter 3, using a quantum circuit model, I show how we emulate the anyonic statistics appears in the 7-qubit system.

In chapter 4 and 5, the basics of NMR QIP and implementation of such a circuit using NMR QIP are described. I describe the molecule, Dicholoro-cyclobutanone, used for the implementation and its internal Hamiltonian, and the thermal state in a NMR setting, measurement, initialization method, control Hamiltonian, and control techniques are discussed. Although these chapters are focused on implementing the sample for this experiment, Dicholoro-cyclobutanone, this discussion can be easily extended to other molecules. Moreover, the experimental protocol used for the experiment is explained in chapter 5.

Chapter 6 and 7 cover the experimental results, and discussion and conclusion, respectively. In particular, I discuss about the effects of gate imperfections and decoherence on the anyonic phases.

Chapter 2

Anyons for Quantum Information Processing

One of the commonly used computational models for quantum computation is a circuit model, which is shown in Figure 2.1. In this model, one starts with a certain initial state and a series of quantum gates are applied to implement a certain algorithm.

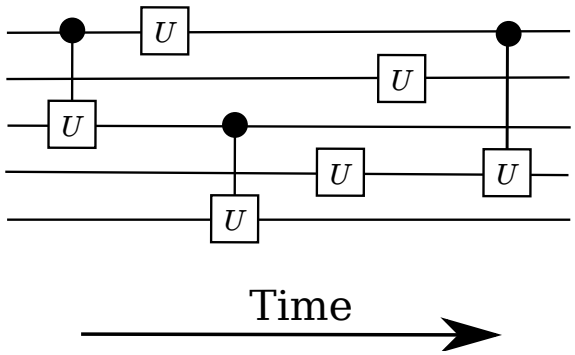

Figure 2.1: Circuit Model Qunutum Computation: computation starts with a certain initial state and a series of gates are applied. In this scheme, time travels horizontally. At the end of the computation, one can measure the final state.

There are also other computation models; one of particular interest to this thesis is topological quantum computation (TQC) using anyons. This scheme is based on the properties of quasi-particle anyons. In this scheme, one starts with a two-dimensional (2D) system, for instance, a lattice of nuclear or electron spins. This 2D system is special such that the quasi-particle anyons (red dots in Figure 2.2 (b)) appear as excitations or defects in the system. Then, rather than

attending to the background system of spins (such as nuclear or electron spins), one can focus on anyons to perform computation by moving them around. In Figure 2.5, time travels vertically and as time advances, the anyons are moved following particular paths to implement a certain algorithm.

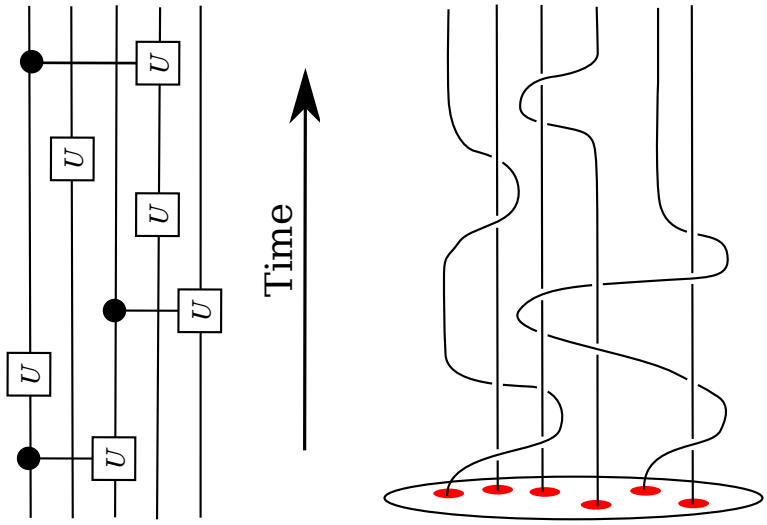

(a) QC (b) TQC

Figure 2.2: (a) Quantum Circuit Model vs (b) Topological Quantum Computing: unlike the circuit model, the gates are implemented by braiding anyons. The anyons are depicted as red dots. The black lines depict the trajectories of the anyons over time, braiding the anyons in specific ways to implement a specific quantum algorithm.

This chapter is concerned with anyons and topological quantum computation.

2.1 What are Anyons?

Anyons are particles that can be created in a 2D system, such as a spin lattice system. They have an unique property which distinguishes them from other fundamental particles, such as bosons or fermions. This property, known as fractional statistics, plays a key role in TQC, allowing implementation of a quantum gate using anyons. The statistical property of interest is how the system's wave function changes when the positions of two indistinguishable particles are

exchanged. Note that unlike bosonic and fermionic cases (Equation 2.1 and 2.2, respectively),

$$P_{ij} \left| N \text{ bosons} \right\rangle = + \left| N \text{ bosons} \right\rangle \tag{2.1}$$

$$P_{ij} \left| N \text{ fermions} \right\rangle = - \left| N \text{ fermions} \right\rangle \tag{2.2}$$

the wave function of anyonic cases can either attain a phase factor, ranging from 0 to 2π (abelian anyon), or evolve according to a unitary matrix [non-abelian anyon] (Equation 2.3 and 2.4, respectively):

$$P_{ij} \left| N \text{ abelian anyons} \right\rangle = e^{i\theta} \left| N \text{ abelian anyons} \right\rangle \tag{2.3}$$

$$P_{ij} \left| N \text{ non-abelian anyons} \right\rangle = U \left| N \text{ non-abelian anyons} \right\rangle , \tag{2.4}$$

where P_{ij} is an exchange operation, exchanging the position of i^{th} and j^{th} particles out of N particles.

This interesting phenomenon results from the topological difference of the exchange operations in 2D and three dimensional (3D) cases. To show the topological difference, we will consider exchanging the particles *twice*. Exchanging the positions of two particles twice is equivalent to moving one particle around the other as shown in Figure 2.3. Such a braiding path can be contracted to a point for a three dimensional case, whereas the braiding path confined on a plane (a 2D case) cannot be contracted to a point (for more detailed explanation, refer to Figure 2.4). Therefore, the braiding paths in the 2D and 3D cases are topologically distinct, giving rise to anyons with non-trivial statistics.

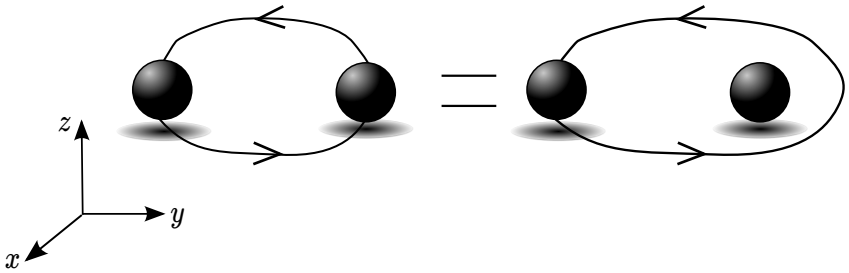

Figure 2.3: The operation that exchanges the particles twice is equivalent to circulating one particle around the other. This is a topological operation which does not depend on a particular shape of the path taken by the particles when they are interchanged. The evolution depends on a global property such as how many times the path circulates one particle.

This operation of exchanging the positions of particles is referred to as a 'braiding operation' [29] in general. In literature, the concept of braiding statistics for anyons are discussed in 2 +

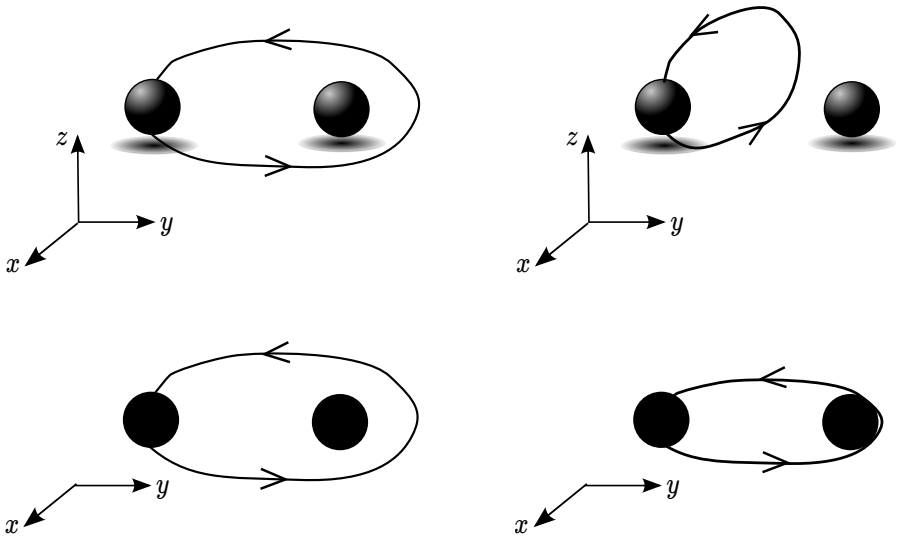

(a) A Braiding Loop in 3D and 2D

(b) Deforming a Braiding Loop in 3D and 2D

Figure 2.4: The topological difference of the braiding path between the three dimensional (top) and the two dimensional (bottom) cases. The braiding path, the black path, can be smoothly deformed to a point for the three dimensional case (imagine the situation where we are pulling one end of the black loop, and we also have freedom to move this loop up and down). This operation is effectively doing nothing on the system. However, in a two dimensional case, since the black loop is confined in a plane, we cannot continuously deform the path to a point (unless we make a cut). Here, again, imagine pulling one end of the black loop, but without the freedom of moving the loop up and down. The loop gets stuck.

1-dimensions with time traversing vertically as shown in Figure 2.2.

Unfortunately, we do not have the ability to build a truly 2D system [15, 29]. However, what we can realize physically is an effective 2D system. Therefore, anyons do not appear as fundamental particles, but as quasiparticles: a group of fundamental particles (such as electron or nuclear spins) collectively behaving as a fundamental particle. These behaviours are usually manifested when the system is excited from the ground state. One could either cause this excitation intentionally or there could be impurities in the system causing the excitations.

2.2 Topological Quantum Computation with Anyons and Its Resilience to Errors

In this section, I will describe a high-level picture of how anyons can be used for quantum computation. Moreover, I will show how natural immunity to errors occurs in this model: this model is known to be protected against both unitary and local errors due to imperfect gate operations and the unwanted interaction with the environments, respectively.

The first step is to realize an 'anyonic system' where the computation takes place. As mentioned before, an anyonic system is a two-dimensional system, and I will focus on a system of many interacting particles (electrons, bosons, atoms, etc) confined on a plane (Figure 2.2). There are a few necessary characteristics that an anyonic system exhibits in general. First of all, these systems have degenerate ground states which constitute an encoding space of computation. This encoding space is non-local, meaning that the information is encoded not only in one particular spin but rather in the state of the entire system. Therefore, local errors cannot alter the encoded information. Second of all, the Hamiltonian of such a system possesses an energy gap between the ground states and the excited states. As it is energetically unfavorable to jump from the ground state to the excited state, information encoded in the degenerate ground states is naturally protected against thermal noise under two conditions: when the temperature of the system is much lower than the energy gap and if the gap is not closed by some perturbation.

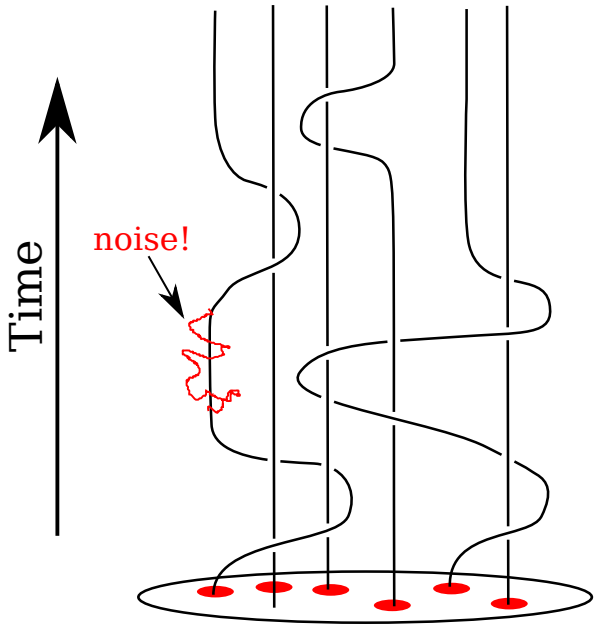

Figure 2.5: Path independence property of anyonic braiding: even when there are local errors which might deform the braiding path with wiggles which are shown in red, the phase gained by the braiding remains the same as long as the anyons are braided.

A third essential characteristic is that an anyonic system carries anyons as excitations or de-

fects that are used for computation. Once we have the ability to create anyons ("initialization of states") from the ground states and move anyons around in specific ways, we can perform controlled unitary operations by braiding anyons, exploiting their exotic statistics as described in Figure 2.2. If the anyons are abelian, then the state evolves to have a phase factor; otherwise it is possible to evolve to have a certain unitary operation, depending on the spin-statistics of the anyons being braided.

Implementing gate operations by braiding anyons is desirable because this procedure is resilient to decoherence. Braiding operations are path independent. It does not matter which paths we use to braid the anyons, as long as the topology of the paths are the same (whether the anyons are braided or not). Thus, the braiding is resilient to local errors which might deform the path with wiggles as shown in Fig 2.5. Secondly, in theory, we ensure that the state evolves exactly by the given anyons' statistics, since the statistics constitute a unique particle property. For instance, if the braiding operation is such that it implements a phase gate by $\pi/2$, the state will evolve to have a $\pi/2$ phase factor exactly, not $\pi/2 \pm \epsilon$ (given that the quantum mechanical description of nature is exact).

In summary, there are three main reasons for resilience to errors.

- Energy gap protecting the ground states, thus protecting the encoded information.
- **Path independence of braiding operation**
- Uniqueness of spin-statistics

In this thesis, we are interested in studying the second property in more detail in a spin-lattice system, in particular, Kitaev's Lattice Model. Thus, we study what it means to have the 'wiggles' in a braiding path in the Kitaev's Lattice Model, and experimentally examine whether the path independence property gives rise to the resilience as expected. Another goal is the proof-of-principle experimental demonstration of such a property.

2.3 Kitaev's Lattice Model

In this model, qubits are located on the edges of a 2D lattice as shown in Figure 2.6 (a). The Hamiltonian of the system contains the two different kinds of four-body interactions, $XXXX$

and $ZZZZ$ (where X and Z are Pauli matrices) at a vertex and plaquette, respectively.

$$H = -\sum_{v} A_v - \sum_{p} B_p, \tag{2.5}$$

where $A_v = \prod_{j \in \text{star}(v)} X_j$, and $B_p = \prod_{j=\text{boundary}(p)} Z_j$. Here, a 'star ($v$)' is a set of four spins that share a link with the vertex v, and a 'boundary (p)' is a set of four spins placed at the edges of the plaquette p (Figure 2.6). The A_v and B_p operators are referred to as stabilizer operators. Since the interactions A_v and B_p commute, the ground state $|\psi_g\rangle$ of this Hamiltonian is a +1 eigenstate of the A_v and B_p operators, $A_v |\psi_g\rangle$

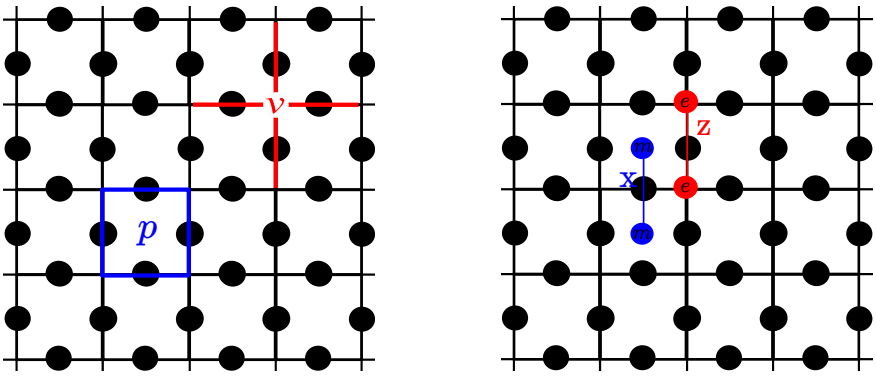

(a) Lattice Model (b) Excitations in Lattice

Figure 2.6: The Kitaev's Lattice Model: (a) the qubits are depicted as circles sitting on the edges on a 2D lattice. There are two different kinds of interactions at a plaquette p and vertex v which describe the Hamiltonian of this system shown in Equation 2.5. (b) the excited states are created by applying single qubit operators X and/or Z. Applying an operator X on a qubit contributes to increasing the energy H by changing the eigenvalues of two of the B_p operators nearby the qubit. Thus, applying an X operator can be depicted as creating two excitations, which are illustrated as the blue dots in the figure, at the particular plaquettes associated with the two B_p that have been excited. Similarly, an operator Z contributes to increasing the energy H by changing the eignvalues of two of the A_v operators nearby the excited qubit, thus, creating excitations (shown in red dots) at the particular vertices. The excitations created on the plaquettes and vertices are called m and e particles, respectively. Moreover, m and e particles possess anyonic statistics with respect to each other.

Note that the interactions $XXXX$ and $ZZZZ$ either have two overlapping qubits or none, thus, the two interaction terms commute. Furthermore, the eigenvalues of $XXXX$ and $ZZZZ$ are ± 1:

$$[A_v, B_p] = 0 \tag{2.6}$$

$$A_v \left|a\right\rangle = \pm \left|a\right\rangle ,\ B_p \left|a\right\rangle = \pm \left|a\right\rangle . \tag{2.7}$$

where $|a\rangle$ is a simultaneous eigenstate of A_v and B_p. Equation 2.6 implies that the eigenstates of A_v and B_p can be constructed such that they share simultaneous eigenstates. Thus, we can analyze the energy spectrum of the Hamiltonian by simply looking at combinations of eigenvalues of A_v and B_p.

Ground State

The ground state(s) of the system is a $+1$ eigenstate(s) of all the A_v and B_p operators, since this is when the lowest energy (E_0) is achieve, where $E_0 = -(N_{A_v} + N_{B_p})$ with N_i indicating number of i operators. Conversely, the highest energy value would be the opposite, having the eigenvalues of -1. Thus, the ground state can be found by projecting the $|0000\cdots0\rangle$ state to a +1 eigenstate of A_v space (note that $|0000\cdots0\rangle$ is already a +1 eigenstate of B_p, so we only need to worry about projecting onto the +1 space of A_v) as the following:

$$|\psi_{\text{ground}}\rangle = \prod_v \left(\frac{I + A_v}{\sqrt{2}}\right) |0000\cdots\rangle \tag{2.8}$$

where $\prod_v \left(\frac{I+A_v}{\sqrt{2}}\right)$ is the projection operator.

Excited States and Anyons

One can excite the ground state to a state with higher energy by taking the ground state out of the $+1$ eigenstate of A_p and B_p. An X or Z operation on a single qubit achieves such an excitation. Suppose there is a Z excitation on the i-th qubit, $Z_i |\psi_{\text{ground}}\rangle$. Then, the state becomes a -1 eigenstate to the operators of A_v, which shares a link with qubit i at the vertex v, thus increasing its energy:

$$XXXX_i(Z_i \left|\psi_{\text{ground}}\right\rangle) = -Z_i(XXXX_i \left|\psi_{\text{ground}}\right\rangle) \tag{2.9}$$
$$= -Z_i \left|\psi_{\text{ground}}\right\rangle, \tag{2.10}$$

where X operators without the subscript indicates X operators on qubits other than i, and I used the anti-commutation relationship between X_i and Z_i. A similar argument applies to Z excitations. These operations that excite the ground state can be viewed as creating defects in the system at a relevant A_v or B_p position: Z excitations create defects on the vertices (since the vertex operators, A_v, are excited) and X excitations create defects on the plaquettes. Defects on the vertices are called 'e' particles and the defects on the plaquette are called 'm' particles. As a result of the geometry of the lattice, e and m particles are always created in a pair per each X and Z excitation as shown in the top right figure of Figure 2.6. Exciting a single qubit with a X or Z excitation excites a pair of B_p or A_v interactions, respectively. Thus, the next energy level increases by +2 with respect to the ground state energy. It can be shown that e and m particles behave as anyons with respect to each other.

Anyonic Statistics

To see that the spin-statistic between e and m particles is indeed anyonic, we can braid a e particle around an m particle (or vice versa). Notice that in this model, we cannot simply exchange the positions of the two particles, since e is located on a vertex and m is located on a plaqutte. Starting with the state $|\psi_i\rangle$ with X_1 and Z_0 excitations on the ground state $|\psi_{\text{ground}}\rangle$ ($|\psi_i\rangle = X_1 Z_0 \left|\psi_{\text{ground}}\right\rangle$), the operation which braids the m particle around the e corresponds to a $X_0X_3X_2X_1$ operation (Figure 2.7). Since $(X)^2 = I$, having two m particles on the top of each other is equivalent to not having a defect (Figure 2.7 (a) (b)). Thus, one can visualize applying the sequence of X operations such as $X_0X_3X_2X_1$ moves the m particle as specified by the braiding operation (Figure 2.7 (c)). Applying the braiding operation on $|\psi_i\rangle$,

$$\begin{aligned} |\psi_f\rangle &= X_0X_3X_2X_1 \left|\psi_i\right\rangle \\ &= X_0X_3X_2X_1[|X_1Z_0] \left|\psi_{\text{ground}}\right\rangle\rangle \\ &= -[X_1Z_0]X_0X_3X_2X_1 \left|\psi_{\text{ground}}\right\rangle \\ &= - \left|\psi_i\right\rangle, \end{aligned} \tag{2.11}$$

$|\psi_i\rangle$ picks up a π phase. Thus, e and m particles behave anyonic with respect to each other, picking up a π phase when they are braided.

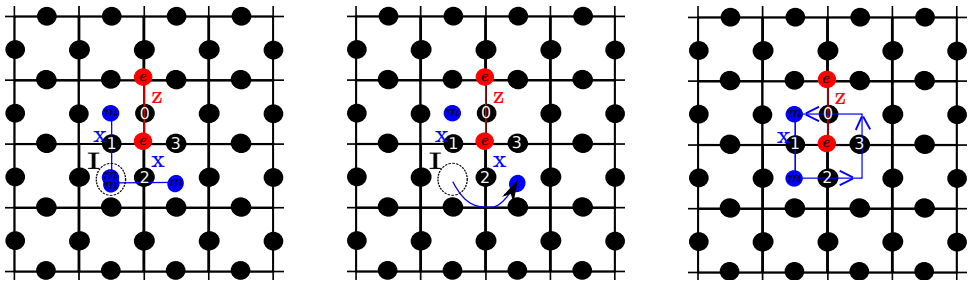

(a) Step 1 (b) Step 2 (c) Step 3

Figure 2.7: Steps of anyonic braiding operations: a pair of e particles were created by exciting qubit 0 and a pair of m particles were created by exciting qubit 1. (a) and (b): applying X to a nearby qubit moves the m particle's location from one plaquette to the other. (c) the full operation which braids a m particle around e is $X_0X_3X_2X_1$.

2.3.1 The 7-qubit Kitaev's Lattice Model

For our experiment, we are interested in a small instance of Kitaev's lattice model: the 7-qubit model which is described in detail in next section. In this model, there are three possible ways to braid the e and m particles around. The trivial braiding loop which does not change the wave function, and the two non-trivial loop which evolve the wave function to gain a phase factor π.

Chapter 3

Theoretical Proposal

The following chapter outlines the theoretical proposal to emulate anyonic physics using a circuit model.

3.1 The 7-qubit Spin-lattice Model in Detail

The 7-qubit model used to demonstrate the path-independence property of anyon braiding is shown in Figure 3.1 (a).

The Hamiltonian of the system (H_7) is,

$$H_7 = -A_1 - A_2 - B_1 - B_2 - B_3 - B_4 - B_5, \tag{3.1}$$

where

$$\begin{gathered} A_1 = X_1X_2X_3X_4, \;\; A_2 = X_4X_5X_6X_7, \\ B_1 = Z_1Z_2, \;\; B_2 = Z_1Z_3, \;\; B_3 = Z_2Z_4Z_5, \\ B_4 = Z_3Z_4Z_6, \quad B_5 = Z_5Z_7 \end{gathered}$$

The ground state $|\psi_{\text{ground}}\rangle$ of this system can be found by projecting the state $|000\cdots0\rangle$ on the +1 eigenstates of the stabilizer operators,

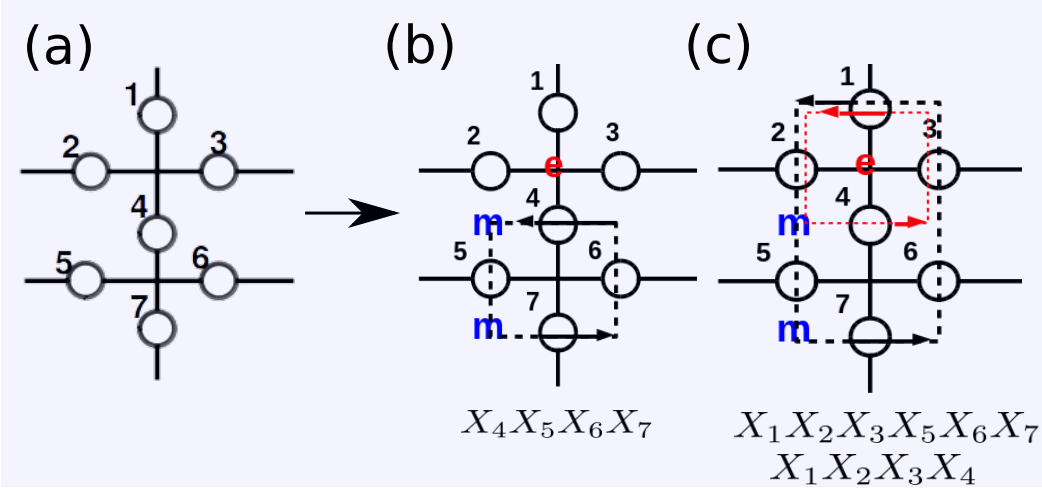

Figure 3.1: The 7-qubit Kitaev Lattice Model: (a) the qubits (circles) are situated on the edges of a 2D lattice. The qubits are subjected to A_v and B_p interactions shown in Equation 3.1 at each vertex and plaquette, respectively. In the figures (b) and (c), an e excitation is created by exciting qubit 1, and m excitations are created by exciting qubit 5. (b) The black loop, $X_4X_5X_6X_7$, represents a trivial loop in which a m particle is moved along the the loop and the system's wave function remains the same. (c) the black and red loops, $X_1X_2X_3X_5X_6X_7$ and $X_1X_2X_3X_4$ respectively, are non-trivial braiding paths which result in a π phase gain of the wave function.

$$
\begin{aligned}
|\psi_{\text{ground}}\rangle &= \prod_{v=1,2} \frac{1}{\sqrt{2}}(I + A_v)\,|0000000\rangle \\
&= \frac{1}{2}(|0000000\rangle + |1111000\rangle + |0001111\rangle + |1110111\rangle).
\end{aligned}
\tag{3.2}
$$

In this model, we create an e particle by exciting qubit 1 and create m particles by exciting qubit 5 (Figure 3.1). This allows for three different loops to move a m particle around in order to explore anyon braiding statistics. The first braiding loop is a trivial loop (l_0), meaning the system wave function remains the same. The other two loops are non-trivial loops (l_1 and l_2), meaning the wave function gains a π phase after braiding.

Demonstrating geometric path independence property of the fractional statistics does not require the Hamiltonian, but only the ground state. The Hamiltonian helps in finding what the ground state is. Therefore, we concentrate on preparing the ground state rather than simulating the Hamiltonian involving A_v, B_p interactions. Therefore, we emulate the braiding operations using

the quantum circuit model. Such idea was first proposed in [11] using a 9-qubit model.

The experimental scheme is to prepare the $|\psi_{\text{ground}}\rangle$ and create a superposition state of

$$(|\psi_{mm}\rangle + |\psi_{mme}\rangle)/\sqrt{2}, \tag{3.3}$$

where $|\psi_{mm}\rangle$ is a state with a pair of m particles created on neighbouring faces of qubit 5, and $|\psi_{mme}\rangle$ represents a state with both an e particle (created by exciting qubit 1) and a pair of m particles (Figure 3.1). After the braiding operation, such a state picks up a partial phase on the $|\psi_{mme}\rangle$ part, if the anyons are braided along a non-trivial loop. Therefore, by measuring this partial phase obtained under the two different non-trivial loops, l_1 and l_2, one can experimentally demonstrate and test geometric path independence property of anyonic braiding.

3.2 Emulation of Anyonic Statistics using the Quantum Circuit

The circuit used to implement the experiments is shown in Figure 3.2.

3.2.1 Mapping the Qubits to Nuclear Spins

We use nuclear spins as the qubits and NMR techniques to implement the above circuit shown in Figure 3.2. In particular, we used the nuclear spins of carbon-13 atoms, and the geometry of the carbons in the molecule is shown in Figure 3.3. It is important to efficiently map each qubit in the circuit to each carbon in the molecule to achieve an optimized circuit. For example, qubit 4 has three CNOT gates with qubit 1, 2 and 3. Therefore, the most desirable carbon to map it to would be C_7 or C_2, since both C_7 and C_2 have three direct bonds to other carbons. The direct bond means higher coupling which indicates it will be faster to implement such two qubit gate. By observing the circuit and looking at the geometry of the molecule, we came up with the mapping illustrated in Figure 3.3.

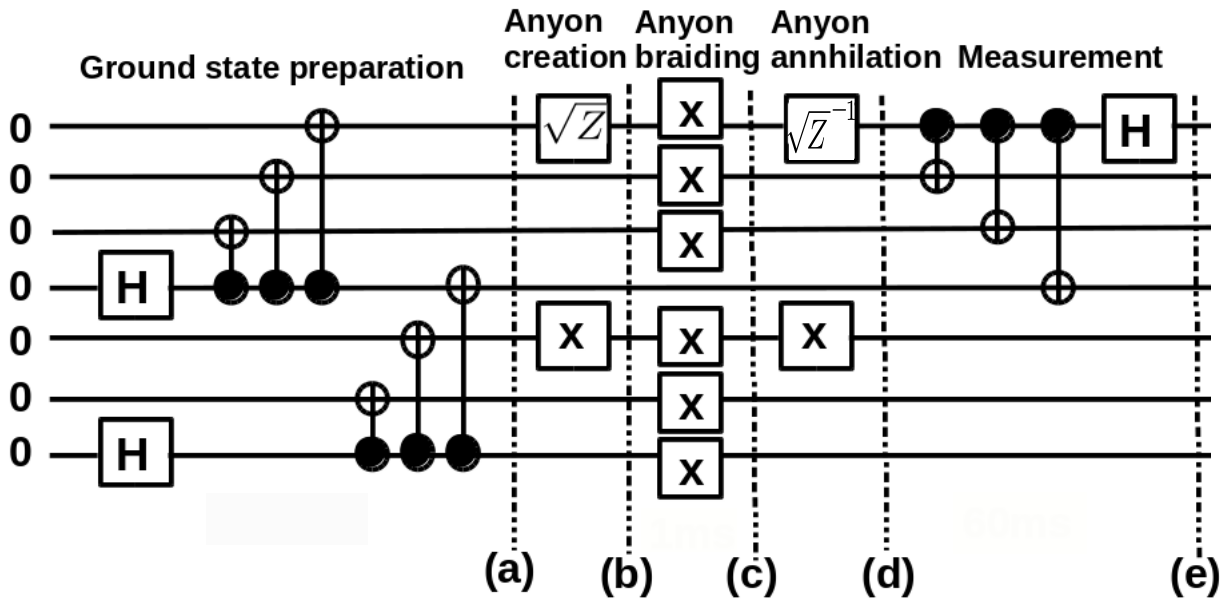

Figure 3.2: The circuit diagram of the emulation: starting with $|0000000\rangle$, the $|\psi_{\text{ground}}\rangle$ is prepared at (a). The subsequent steps are the anyonic manipulation procedure: (b) the superposition state (Equation 3.3) is created, (c) the anyons are braided, and (d) the anyons are annihilated. The subsequent measurement gate is added to change the basis such that the anyonic phases can be evaluated.

The states corresponding to each step of the circuit shown in Figure 3.2:

$$\begin{aligned}
|\psi_{\text{a}}\rangle &= |\psi_{\text{ground}}\rangle \\
&= \frac{1}{2}(|0_{\text{C4}}0_{\text{C6}}0_{\text{C5}}0_{\text{C7}}0_{\text{C1}}0_{\text{C3}}0_{\text{C2}}\rangle \\
&\quad + |1_{\text{C4}}1_{\text{C6}}1_{\text{C5}}1_{\text{C7}}0_{\text{C1}}0_{\text{C3}}0_{\text{C2}}\rangle \\
&\quad + |0_{\text{C4}}0_{\text{C6}}0_{\text{C5}}1_{\text{C7}}1_{\text{C1}}1_{\text{C3}}1_{\text{C2}}\rangle \\
&\quad + |1_{\text{C4}}1_{\text{C6}}1_{\text{C5}}0_{\text{C7}}1_{\text{C1}}1_{\text{C3}}1_{\text{C2}}\rangle)
\end{aligned} \tag{3.4}$$

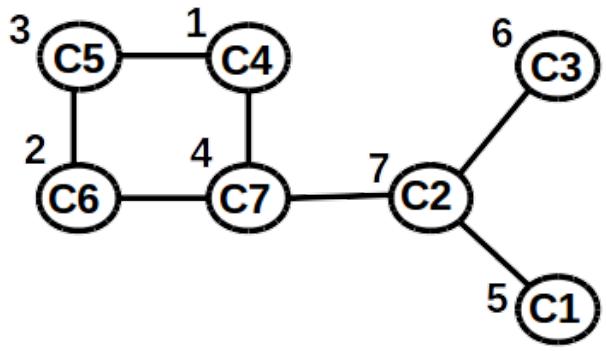

Figure 3.3: Mapping of the qubits shown in Figure 3.2 to the carbon spins in the molecule used for the implementation: there are seven distinguishable carbon spins in the molecule, and the spins are depicted as the circles with labelling of C1, C2, C3, C4, C5, C6 and C7. The geometry of the graph reflects the geometry of the carbon spins in the molecule. The numbering written on the top left corner of each carbon represents the qubit that it is mapped to. For instance, C5 represents qubit 3.

$$
\begin{aligned}
|\psi_{\mathrm{b}}\rangle =& \frac{e^{i\pi/4}}{\sqrt{2}}(X_5 |\psi_{\text{ground}}\rangle - iZ_1X_5 |\psi_{\text{ground}}\rangle) \\
=& \frac{e^{i\pi/4}}{\sqrt{2}}(|\psi_{mm}\rangle - i |\psi_{mme}\rangle) \\
=& \frac{1}{2}(|0_{\mathrm{C4}}0_{\mathrm{C6}}0_{\mathrm{C5}}0_{\mathrm{C7}}1_{\mathrm{C1}}0_{\mathrm{C3}}0_{\mathrm{C2}}\rangle \\
&+ \mathrm{i}\,|1_{\mathrm{C4}}1_{\mathrm{C6}}1_{\mathrm{C5}}1_{\mathrm{C7}}1_{\mathrm{C1}}0_{\mathrm{C3}}0_{\mathrm{C2}}\rangle \\
&+ |0_{\mathrm{C4}}0_{\mathrm{C6}}0_{\mathrm{C5}}1_{\mathrm{C7}}0_{\mathrm{C1}}1_{\mathrm{C3}}1_{\mathrm{C2}}\rangle \\
&+ \mathrm{i}\,|1_{\mathrm{C4}}1_{\mathrm{C6}}1_{\mathrm{C5}}0_{\mathrm{C7}}0_{\mathrm{C1}}1_{\mathrm{C3}}1_{\mathrm{C2}}\rangle)
\end{aligned}
\tag{3.5}
$$

$$
\begin{aligned}
|\psi_{\text{c}}\rangle =& \frac{e^{i\pi/4}}{\sqrt{2}}(X_5 |\psi_{\text{ground}}\rangle - ie^{i\theta} Z_1 X_5 |\psi_{\text{ground}}\rangle) \\
=& \frac{e^{i\pi/4}}{\sqrt{2}}(|\psi_{mm}\rangle - ie^{i\theta} |\psi_{mme}\rangle) \\
=& \frac{e^{i\pi/4}}{2\sqrt{2}}\Big((1 - ie^{i\theta})|0_{\text{C4}}0_{\text{C6}}0_{\text{C5}}0_{\text{C7}}1_{\text{C1}}0_{\text{C3}}0_{\text{C2}}\rangle \\
&+ (1 + ie^{i\theta})|1_{\text{C4}}1_{\text{C6}}1_{\text{C5}}1_{\text{C7}}1_{\text{C1}}0_{\text{C3}}0_{\text{C2}}\rangle \\
&+ (1 - ie^{i\theta})|0_{\text{C4}}0_{\text{C6}}0_{\text{C5}}1_{\text{C7}}0_{\text{C1}}1_{\text{C3}}1_{\text{C2}}\rangle \\
&+ (1 + ie^{i\theta})|1_{\text{C4}}1_{\text{C6}}1_{\text{C5}}0_{\text{C7}}0_{\text{C1}}1_{\text{C3}}1_{\text{C2}}\rangle\Big)
\end{aligned} \tag{3.6}
$$

$$
\begin{aligned}
|\psi_{\text{d}}\rangle =& \frac{1}{2}((I + e^{i\theta}) |\psi_{\text{ground}}\rangle + i(I - e^{i\theta}) Z_1 |\psi_{\text{ground}}\rangle) \\
=& \frac{1}{2}((I + e^{i\theta}) |\psi_{\text{ground}}\rangle + i(I - e^{i\theta}) |\psi_{\text{excited}}\rangle)
\end{aligned} \tag{3.7}
$$

where the subscript of each qubit indicates the carbon that the qubit is mapped to[1], $|\psi_{mm}\rangle = X_5 |\psi_{\text{ground}}\rangle$ and $|\psi_{mme}\rangle = Z_1 X_5 |\psi_{\text{ground}}\rangle$.

Let $\alpha = (1 + e^{i\theta})/2\sqrt{2}$ and $\beta = i(1 - e^{i\theta})/2\sqrt{2}$. Then

[1]Throughout the thesis, if there is no subscript on a state, a state is written following the order of the qubits in the emulation circuit (Figure 3.2). For instance, $|010000\rangle$ presents $|0\rangle$ for qubit 1 and 3-7, thus, C4,C5,C7,C1,C3, and C7, and $|1\rangle$ for the qubit 2, thus, C6. Refer to Figure 3.3 for the qubit to carbon mapping.

$$\begin{aligned}\frac{\beta}{\alpha} &= i\frac{1-e^{i\theta}}{1+e^{i\theta}} \\ &= i\frac{e^{-i\theta/2}-e^{i\theta/2}}{e^{-i\theta/2}+e^{i\theta/2}} \\ &= i\frac{\sin(\theta/2)}{\cos(\theta/2)} \\ &= i\tan(\theta/2),\end{aligned}$$

leading to

$$\theta_{\text{anyon}} = 2\arctan\left(\sqrt{\left|\frac{\beta}{\alpha}\right|^2}\right), \quad -\pi < \theta < \pi. \tag{3.8}$$

Therefore, by measuring the diagonal elements $|0000000\rangle\langle 0000000|$ or $|0001111\rangle\langle 0001111|$ and $|1000000\rangle\langle 1000000|$ or $|1001111\rangle\langle 1001111|$, it is possible to evaluate $|\alpha|^2$ and $|\beta|^2$ respectively, such that θ_{anyon} can be determined. Theoretically, $\theta_{\text{anyon}} = 0$ for the trivial loop l_0 which is the case when $\beta = 0,\ \alpha = 1/\sqrt{2}$, leading to $\theta_{\text{anyon}} = 2\arctan(0) = 0$. For the non-trivial loops, l_1 and l_2, $\theta_{\text{anyon}} = \pi$ which are the cases when $\beta = i/\sqrt{2},\ \alpha = 0$, thus, $\theta = 2\arctan(\infty) = \pi$.

Chapter 4

Basics of NMR QIP

The primary resource used for this chapter is [23].

4.1 NMR Systems

In liquid-state NMR systems, a sample contains a large number, a number close to Avogadro's number ($10^{15} \sim 10^{16}$), of identical and non-interacting molecules in a liquid state. Each molecule acts a single quantum information processor. Thus, NMR QIP performs ensemble computation: applying a gate simultaneously to many identical devices and measuring an average of the ensemble's output. Atoms with an odd number of protons in the molecule can be used as qubits when the sample is placed in an external magnetic field, which is typically defined to be applied along the $\overrightarrow{Z}$ direction. For our experiment, we used dichloro-cyclobutanone, which is a molecule with seven C-13 labelled carbon atoms and five hydrogen atoms. Unless explicitly mentioned, it is assumed that the carbon atoms and hydrogen atoms are decoupled throughout the thesis, since we only need seven qubits to emulate the circuit of interest (Figure 3.2) and we indeed decoupled them for the majority of the experiment.

4.1.1 Natural Hamiltonian

To manipulate the nuclear spins of a molecule, one needs to be able to characterize the nuclear spins' dynamics under time evolution. Thus, it is necessary to know the system Hamiltonian. The natural nuclear spin-1/2 Hamiltonian in liquid-state NMR systems is given by

$$H_{\text{nat}} \approx \sum_i \omega_i Z_i + \sum_{i<j} 2\pi J_{ij} Z_i Z_j, \tag{4.1}$$

where $\omega_i = \gamma_i(1+\delta_i)|\overrightarrow{B_0}|$ is the Larmor frequency of the i^{th} spin with gyromagnetic ratio γ_i and chemical shift δ_i. The gyromagnetic ratio is the same between the same isotopes of nuclear spins; however, the chemical shifts δ_i are different even between same isotopes. J_{ij} is the coupling strength between the i^{th} and j^{th} spins. The first term results from the interaction between the nuclear spin and the external magnetic field of strength B_0, causing the Zeeman splitting of the levels $|0\rangle$ and $|1\rangle$. On the top of the Zeeman interaction, the external magnetic field induces currents in the electron clouds which again induces a small magnetic field. Although the induced magnetic field is typically only around 10^{-4} of the external magnetic field, it is sufficient to observe this shift in frequency δ_i experimentally. The spins with asymmetric geometry are exposed to different electronic environments. Therefore, for such spins, the chemical shift is different for each spin, even between homo-nuclear spins. The second term originates from the indirect magnetic interactions through the hyperfine interaction between nuclear and electron spins.

It might be surprising that the natural Hamiltonian is relatively simple, considering that there are a large number of electrons present along with nuclear spins. Nuclear spins in NMR systems are in a special situation where some interaction terms can be neglected or simplified through the next four approximations. First, the spin Hamiltonian hypothesis that the electronic motion is much faster than the nuclear spins is made. This means that nuclear spins only sense a time average of the fields that electrons generate. A second consideration is that the energy of the nuclear spins is too small to influence the motion of electrons. Third, the secular approximation that the dynamics are largely dominated by $\overrightarrow{B_0}$ reduces J-coupling interaction term from $X_iX_j + Y_iY_j + Z_iZ_j$ to Z_iZ_j. This is called a weak coupling approximation and our 7-qubit system can be treated in this regime. Fourth, in liquid state NMR, a rapid molecular motion averages intramolecular dipole-dipole interactions. Intermolecular dipole-dipole interactions do not average out completely; however, they are very small compared to other couplings. This long ranged dipole-dipole interaction that does not average out contributes in decoherence phenomena which is discussed in Section 4.1.4.

The Hamiltonian parameters of dichloro-cyclobutanone molecule is shown in Figure 4.1. Note that the J-coupling constants, ranging from 30Hz to 60Hz, are larger between the carbons connected by covalent bonds than the carbons that are far apart.

4.1.2 Thermal State

When the ensemble of spins is left undisturbed for a sufficiently long time, it reaches thermal equilibrium state. The thermal state ρ_{th} of the molecule obeys the Boltzmann distribution,

$$\rho_{\text{th}} = \frac{e^{-\beta H_{\text{nat}}}}{\text{Tr}(e^{-\beta H_{\text{nat}}})} \tag{4.2}$$

where β is 1/(k_BT) with the Boltzmann constant k_B and temperature T. Since the Zeeman energies (which arise from the dominating term in H_{nat}) of the spins are much smaller than k_BT at room temperature, the thermal state can be approximated to:

$$\rho_{\text{th}} \approx \frac{I}{2^N} + \frac{B}{2^N} \sum_{i=1}^{N} \frac{Z_i}{2} \tag{4.3}$$

where N is the number of spins, and $B = \hbar\gamma\beta B_0$ is the Boltzmann factor. Therefore, the thermal state of the dichloro-cyclobutanone molecule is (neglecting hydrogen atoms):

$$\rho_{\text{th}} \approx \frac{I}{2^N} + \frac{B}{2^{N+1}} \left(Z_{C_1} + Z_{C_2} + Z_{C_3} + Z_{C_4} + Z_{C_5} + Z_{C_6} + Z_{C_7} \right) \tag{4.4}$$

B is about 10^{-5} at room temperature, thus, the state is highly mixed. In the NMR QIP community, a deviation matrix $\widetilde{\rho} = \rho - I/2^N$ is used rather than ρ, since the identity part does not evolve under unitary transformation, nor it contributes to the NMR signal[1]. Thus, we can express the renormalized thermal state as $\widetilde{\rho}_{\text{th}} = Z_{C_1} + Z_{C_2} + Z_{C_3} + Z_{C_4} + Z_{C_5} + Z_{C_6} + Z_{C_7}$.

[1] For the rest of the thesis, any state of the form $\widetilde{\rho}$ is a deviation density matrix of ρ.

	C1	C2	C3	C4	C5	C6	C7	H1	H2	H3	H4	H5
C1	30020											
C2	57.58	8779										
C3	-2.00	32.70	6245									
C4	0	0.30	0	10333								
C5	1.25	2.62	-1.11	33.16	15745							
C6	5.54	-1.66	0	-3.53	33.16	34381						
C7	-1.25	37.48	0.94	29.02	21.75	34.57	11928					
H1	0	0	2.36	166.6	4.06	5.39	8.61	3310				
H2	4.41	1.86	146.6	2.37	0	0	0	0	2468			
H3	1.81	3.71	146.6	2.37	0	0	0	0.18	-12.41	2158		
H4	-13.19	133.6	-6.97	6.23	0	5.39	3.78	-0.68	1.28	6.00	2692	
H5	7.87	-8.35	3.35	8.13	2.36	8.52	148.5	8.46	-1.06	-0.36	1.30	3649
T1	8.015	3.611	1.834	3.722	12.95	8.157	3.636	3.831	2.128	2.278	2.654	3.472
T2	1.611	0.877	1.122	0.792	1.143	1.912	0.531	0.337	N/A	N/A	0.318	0.276

C-13 labeled 12-qubit system

Dichloro–cyclobutanone

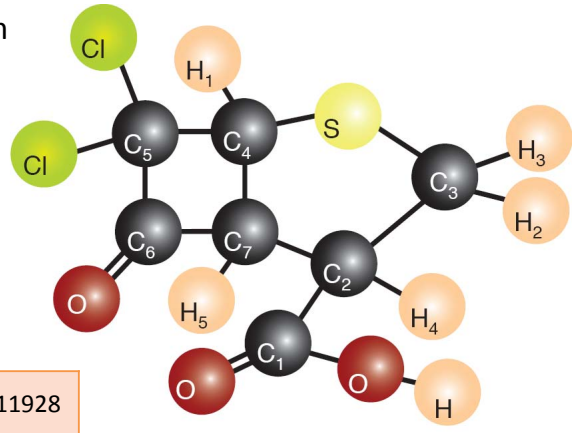

Figure 4.1: The sample Hamiltonian: the top right figure shows the molecular structure of dichloro-cyclobutanone. For our experiments, we only use the carbon nuclear spins as qubits (the hydrogen were decoupled). The parameters ω_i and J_{ij} (Hz) which characterize the Hamiltonian Equation 4.1 are shown in the diagonal and off-diagonal elements of the chart. T1 and T2, which are phenomenological relaxation constants that characterize decay of diagonal and off-diagonal elements of density matrix, respectively, are also shown in unit second (T1 decay also affect off-diagonal terms; however, the decay of off-diagonal elements are mostly dominated by the T2 decay rate).

4.1.3 NMR Measurement

When the sample is disturbed from the thermal equilibrium state, precessing magnetization of the sample can be detected by the coil placed perpendicularly to the external magnetic field. According to Faraday's law, the induced emf (V) in the coil is proportional to the the total magnetic flux (Φ) in the coil:

$$V(t) \propto \frac{d\Phi}{dt} \propto \frac{dM_x}{dt} = \omega_i M_T \text{cos}(\omega_i t) + \frac{dM_T}{dt}\text{sin}(\omega_i t) \tag{4.5}$$

$$\approx \omega_i M_T \text{cos}(\omega_i t), \tag{4.6}$$

where $M_x = M_T \text{sin}(\omega_i t)$ is magnetization in the X-direction, M_T is the transverse magnetization, and ω_i is the precession frequency of M_T. The second term $\frac{dM_T}{dt}$ is orders of magnitude smaller than the first term. Thus, the NMR signal known as the free induction decay (FID) is dominated by magnitude of precessing transverse magnetization. The precession frequency ω_i is the Larmor frequency, thus, the magnitude of the signal is quadratic in B_0: $|\overrightarrow{V}| \propto |\overrightarrow{B_0}|^2$. In modern NMR spectrometers, quadrature detection techniques allow measurement of both $M_T \text{cos}(\omega_i t)$ and $M_T \text{sin}(\omega_i t)$ components using a phase shifter. Therefore, the signal detected is

$$s(t) \propto \text{Tr}\left[\rho(t) \sum_j (X_j - iY_j)\right], \tag{4.7}$$

where X_j and Y_j are the Pauli X and Y matrices at the j^{th} qubit. Since all the molecules are identical and non-interacting, the above expression only considers a signal from a single spin. It is implicit that the total magnetization is from the sum of all the molecules in a sample ($S_{\text{total}} = NS(t)$, where N is the total number of molecules). Note that the signal from a single spin would be $|\overrightarrow{V}| \propto BB_0 = \hbar\gamma\beta|\overrightarrow{B_0}|^2 = 10^{-5}B_0$, which is too small to be detectable at room temperature. Therefore, ensemble measurement is necessary. Even with ensemble measurement, the signal is further amplified using electronics in spectrometers.

The FID signal is Fourier transformed to the frequency domain for analysis:

$$S(\omega) = \int_0^\infty s(t)e^{i\omega t}dt \tag{4.8}$$

$$= \sum_j \int_0^\infty Tr\left[\rho(t)(X_j - iY_j)\right]e^{i\omega t}dt, \tag{4.9}$$

where the sum is over the qubits. The Fourier transform (FT) of the FID results in 2^{n-1} peaks in the spectra for each X_j given that all the couplings between the qubits can be resolved, where each peak gives information about elements of the density matrix corresponding to (-1) single coherences: with the amplitude and phase of each peak, one can estimate a density element of the form $|k\rangle\langle k|(|0\rangle\langle 1|)_i$ where k is a state in the computational basis. In other words, one can infer expectation values of product operators with only one σ_{x_j} or σ_{y_j} such as $I_{z_{j-1}}\sigma_{x_j}\sigma_{z_{j+1}}$ by taking a linear combination of peak coefficients (where I_z is the spin matrix along the z direction). I will give a two-qubit example of NMR spectra, which can be extended to multi-qubit cases.

For a two-qubit case, the natural Hamiltonian is:

$$H_{\text{nat}} = \omega_1 I_z^1 + \omega_2 I_z^2 + 2\pi J_{12} I_z^1 I_z^2 \tag{4.10}$$

For simplicity, let us consider observing only the first qubit. First, define

$$U_z = e^{-i(\omega_1 I_z^1 + \omega_2 I_z^2)} \tag{4.11}$$

$$U_c = e^{-i2\pi J_{12} I_z^1 I_z^2} \tag{4.12}$$

$$U_z^\dagger I_-^1 U_z = e^{-i\omega_1 t} I_-. \tag{4.13}$$

Then, we have

$$\begin{aligned}
s(t) =& \text{tr}(\rho(t)I_-^1) = \text{tr}(\rho_0 U_c^\dagger U_z^\dagger (I_-^1) U_z U_c) \\
=& e^{-i\omega_i t}\text{tr}(\rho_0 U_c^\dagger I_-^1 U_c) \\
=& \frac{1}{2}e^{-i\omega_1 t}\text{tr}(\rho_0[(I_-^1 - 2I_-^1 I_z^2)e^{i\pi J_{12}t} + (I_-^1 + 2I_-^1 I_z^2)e^{-i\pi J_{12}t}]) \\
=& \frac{1}{2}e^{i(-\omega_1 + \pi J_{12})t}\text{tr}(\rho_0[I_-^1 - 2I_-^1 I_z^2]) \\
& + e^{i(-\omega_1 - \pi J_{12})t}\text{tr}(\rho_0[I_-^i + 2I_-^1 I_z^2]),
\end{aligned}$$

if I include a decay factor $\lambda = 1/\mathrm{T}_2$ from decoherence effect, which is discussed in the next section,

$$\begin{aligned} s(t) =& \frac{1}{2} e^{[i(-\omega_1+\pi J_{12})-\lambda]t} \mathrm{tr}(\rho_0[I_-^1 - 2I_-^1 I_z^2]) \\ &+ e^{[i(-\omega_1-\pi J_{12})-\lambda]t} \mathrm{tr}(\rho_0[I_-^1 + 2I_-^1 I_z^2]) \end{aligned}$$

Fourier transforming the FID signal to get the NMR spectra,

$$\begin{aligned} S(\omega) =& \frac{1}{2}\left(\int_0^\infty e^{i\omega t} e^{[i(-\omega_1+\pi J_{12})-\lambda]t} dt \right) \mathrm{tr}(\rho_0[I_-^1 - 2I_-^1 I_z^2]) \\ &+ \frac{1}{2}\left(\int_0^\infty e^{i\omega t} e^{[i(-\omega_1-\pi J_{12})-\lambda]t} dt \right) \mathrm{tr}(\rho_0[I_-^1 + 2I_-^1 I_z^2]) \\ =& \frac{1}{2}\left(\frac{e^{[i(-\omega_1+\pi J_{12}+\omega)-\lambda]t}}{i(-\omega_1+\pi J_{12}+\omega)-\lambda} \Big|_0^\infty \right) \mathrm{tr}(\rho_0[I_-^1 - 2I_-^1 I_z^2]) \\ &+ \frac{1}{2}\left(\frac{e^{[i(-\omega_1-\pi J_{12}+\omega)-\lambda]t}}{i(-\omega_1-\pi J_{12}+\omega)-\lambda} \Big|_0^\infty \right) \mathrm{tr}(\rho_0[I_-^1 + 2I_-^1 I_z^2]) \\ =& \frac{1}{2}\left(\frac{1}{i(\omega_1-\pi J_{12}-\omega)+\lambda} \right) \mathrm{tr}(\rho_0[I_-^i - 2I_-^1 I_z^2]) \\ &+ \frac{1}{2}\left(\frac{1}{1(\omega_1+\pi J_{12}-\omega)-\lambda} \right) \mathrm{tr}(\rho_0[I_-^1 + 2I_-^1 I_z^2]) \end{aligned}$$

We can separate the real and imaginary parts of the above expression,

$$S(\omega) \propto (A_1 + iD_1)\mathrm{tr}(\rho_0[I_-^1 - 2I_-^1 I_z^2]) + (A_2 + iD_2)\mathrm{tr}(\rho_0[I_-^1 + 2I_-^1 I_z^2]), \tag{4.14}$$

$$= (A_1 + iD_1)\mathrm{tr}(\rho_0[I_-^1 |1\rangle\langle 1|]) + (A_2 + iD_2)\mathrm{tr}(\rho_0[I_-^1 |0\rangle\langle 0|]), \tag{4.15}$$

$$\text{where} \qquad A_i = \frac{1}{(\omega-\omega_i^p)^2+\lambda^2}, \text{ and } \quad D_i = \frac{(\omega-\omega_i^p)}{(\omega-\omega_i^p)^2+\lambda^2} \tag{4.16}$$

with $\omega_1^p = \omega_1 - \pi J_{12}$, $\omega_2^p = \omega_1 + \pi J_{12}$, and A_i and D_i are called absorption and dispersion peaks, respectively. One can easily see that the peaks at frequency (in rad) $\omega_1 \pm \pi J_{12}$ are associated with $I_-^1 |0\rangle\langle 0|$ and $I_-^1 |1\rangle\langle 1|$, respectively. Alternatively, one can rewrite in terms of Pauli matrices, and, taking linear combinations of coefficients of the peaks yield, the expectation of the appropriate Pauli matrix. This is evident when Equation 4.16 is re-written in term of Pauli

matrices:

$$
\begin{aligned}
S(\omega) \propto\ & (A_1 + iD_1)\text{tr}(\rho_0[X(I-Z) - iY(I-Z)]) + (A_2 + iD_2)\text{tr}(\rho_0[X(I+Z) - iY(I+Z)]) \\
=\ & (A_1 + iD_1 + A_2 + iD_2)\text{tr}(\rho_0[XI]) \\
& + (-A_1 - iD_1 + A_2 + iD_2)\text{tr}(\rho_0[XZ]) \\
& - i(+A_1 + iD_1 + A_2 + iD_2)\text{tr}(\rho_0[YI]) \\
& - i(-A_1 - iD_1 + A_2 + iD_2)\text{tr}(\rho_0[YZ])
\end{aligned}
$$

Extending this analysis for the decoupled dichloro-cyclobutanone molecule, the NMR signal of $\widetilde{\rho} = X_{C_7}$ results experimentally in the below spectra (Figure 4.2), where 64 peaks can be resolved: Simulation of the spectra of $\widetilde{\rho} = \sum_i^7 X_{C_i}$ shown in Figure 4.3 indicates that it is not

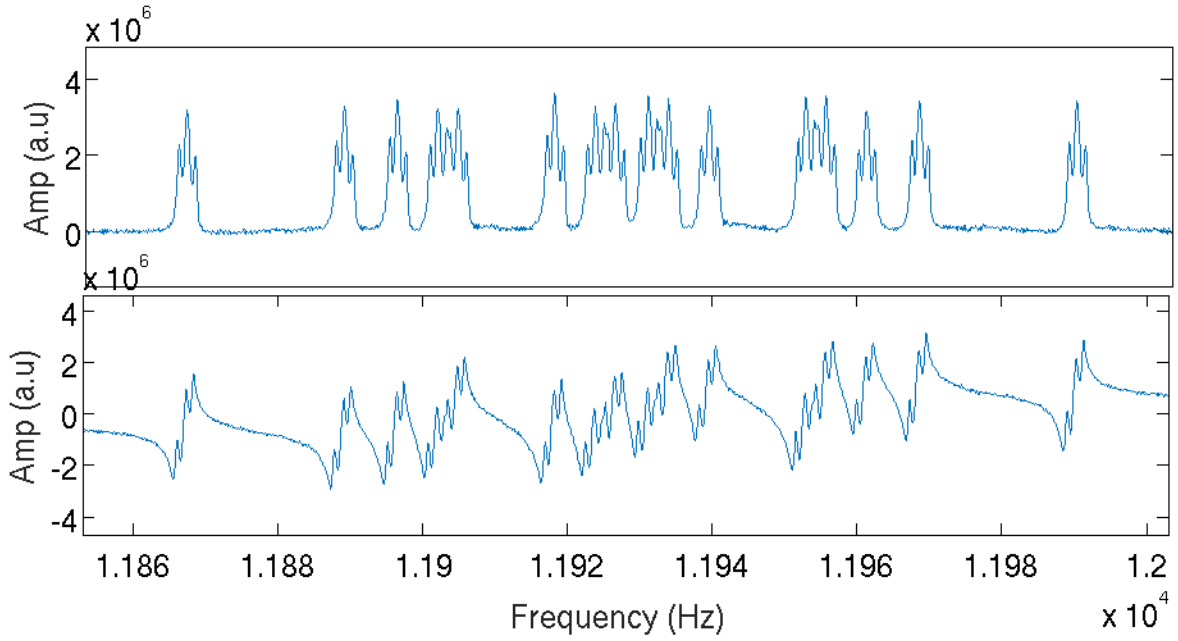

Figure 4.2: The experimental real (top) and imaginary (bottom) parts of the C_7 spectrum of $\widetilde{\rho} = X_{C_7}$. The x-axis indicates the frequency where the center of the frequency matches the Larmor frequency of C_7, and y-axis indicates the amplitude of the peaks. The raw values of amplitudes do not have much physical significance as the FID signal is amplified using electronics in a spectrometer. It is the relative values that are important, therefore, for the rest of this thesis, the amplitudes of a spectrum is normalized relative to a reference amplitude.

always possible to resolve all the couplings for some carbons, resulting in less than 64 peaks for

those carbons.

4.1.4 Decoherence

The two major decoherence phenomena in NMR systems are amplitude damping and dephasing which are characterized by the time constants T_1 and T_2, respectively. T_1 characterizes the time it takes for the spins to re-thermalize to a thermal equilibrium state. When the same measurements are repeated back to back, it is customary to wait $5T_1$ in between the scans to ensure that one starts with the same initial state for the second scan. T_2 characterizes the exponential decay rate of coherence terms (off-diagonal elements of ρ). Indeed, the decay of FID signal is mainly due to T_2 effect. T_2^*, which is the decay mainly due to external factors such as field in-homogeneities, also plays a role; however, the effect of T_2^* can be refocused whereas T_2 effects are intrinsic losses in the coherence terms which cannot be reversed. The mechanisms which cause T_2 effects are the interaction terms that are neglected in the natural Hamiltonian because they are small or average to zero on long time scales such as translational molecular motion and intramolecular dipole-dipole interaction; however, they contribute to decoherence effects by causing fluctuations in the magnetic fields.

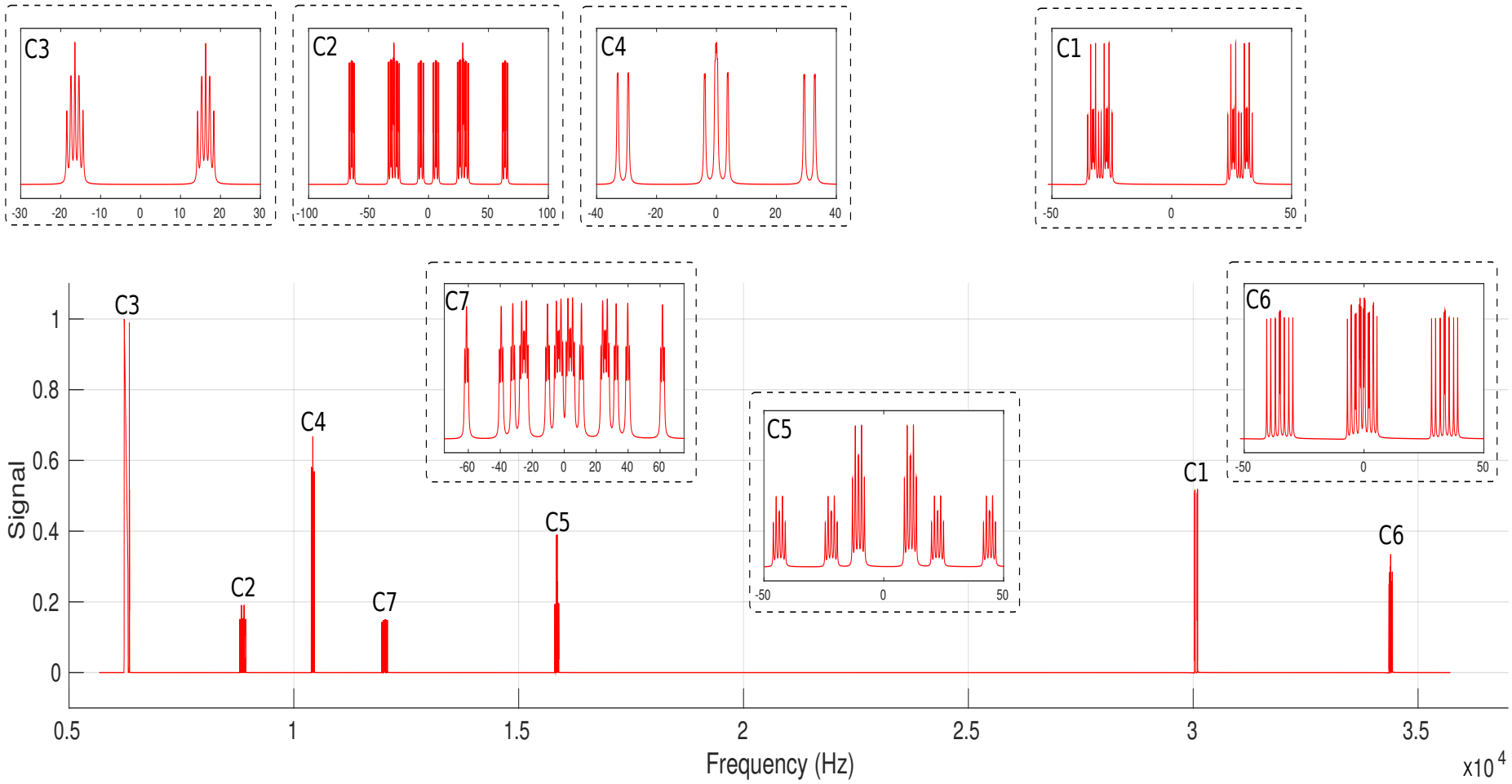

Figure 4.3: Decoupled thermal spectrum of carbon atoms (7-qubit system): the spectrum of each carbon is zoomed out with the frequency centered at its ω_{C_7} value as shown in Figure 4.1.

4.2 Initialization - Pseudo-Pure State (PPS)

In QIP, a state is typically initialized to the pure state $|000\cdots0\rangle$ before computation starts. However, in NMR QIP, the situation is different as it is difficult to prepare a pure state from the thermal equilibrium state which is highly mixed at room temperature. Thus, instead of preparing a pure state, a pseudo-pure state (PPS) is prepared:

$$\rho_{\text{PPS}} = (I - \epsilon)\frac{I}{2^n} + \epsilon\,|000\cdots0\rangle\langle000\cdots0| \tag{4.17}$$

$$\widetilde{\rho}_{\text{PPS}} = |000\cdots0\rangle\langle000\cdots0| \tag{4.18}$$

Although a PPS is not a pure state, the deviation density matrix of a PPS simulates the dynamics of a pure state, i.e, its evolution is given by a quantum Hamiltonian, and also the identity part is undetectable.

There are several different methods to prepare a PPS such as the temporal averaging, spatial averaging, and cat-state methods. All the techniques employ non-unitary transformations. For our experiment, we use the cat-state method [18]. This method consists of three steps:

- Encoding: $Z_{C_7} \rightarrow Z_{C_1}Z_{C_2}Z_{C_3}Z_{C_4}Z_{C_5}Z_{C_6}Z_{C_7}$
- Phase Cycling: $X_{C_1}X_{C_2}X_{C_3}X_{C_4}X_{C_5}X_{C_6}X_{C_7} \rightarrow |0000000\rangle\langle1111111| + |1111111\rangle\langle0000000|$
- Decoding: $|0000000\rangle\langle1111111| + |1111111\rangle\langle0000000| \rightarrow |000000\rangle\langle000000|\,Z_{C_7}$

The phase cycling part selects 7-coherence terms. To achieve such task, multiple scans are averaged to cancel unwanted coherences. Note that in our experiment, we prepared $|000000\rangle\langle000000|\,Z_{C_7}$, which is referred to as labelled PPS, instead of $|0000000\rangle\langle0000000|$, since it is experimentally more challenging to prepare $|0000000\rangle\langle0000000|$.

4.3 NMR Control & Control Techniques

4.3.1 Control Hamiltonian

With the natural Hamiltonian, it is possible to implement single qubit Z rotations or two qubit controlled-Z gates. However, these operations are not sufficient for universal quantum computation. Therefore, it is necessary to be able to implement rotations along a different axis. This is

achieved by applying an oscillating radio-frequency (rf) field of the form:

$$H_{\text{rf}} \cong -\frac{1}{4}\gamma B_{\text{RF}}[\cos(\omega_{\text{ref}}t + \phi_p)\sum_i X_i + \sin(\omega_{\text{ref}}t + \phi_p)\sum_i Y_i] \tag{4.19}$$

where ω_{ref} is the freqency of the rf field, and B_{RF} and ϕ_p are the strength and phase of the field, respectively. Therefore, the total Hamiltonian including both natural Hamiltonian and external Hamiltonian in a rotating frame ω_{ref} is

$$\widetilde{H}_{\text{tot}} \propto \sum_i(\omega_0^i - \omega_{\text{ref}})Z_i + \sum_{i,j}\pi J_{ij}Z_iZ_j + \omega_{\text{nut}}[\cos(\phi_p)\sum_i X_i + \sin(\phi_p)\sum_i Y_i]. \tag{4.20}$$

The frequency of the rf pulse ω_{ref} is chosen such that it is in resonance with the qubits of interest. The strength of the fields ω_{nut} typically ranges up to 30kHz. The phase ϕ_p is relative to the reference scan. Therefore, it is necessary to define the axis in the beginning of experiments. In principle, it is possible to implement any single-qubit and two-qubit gate with such a Hamiltonian; however, this does not imply that searching for desirable pulses IS trivial. For example, when the Larmor frequencies of spins are close by, the excitation profile of the pulse should be narrow to control individual spins. However, such a requirement implies a long pulse. Thus, not only does pulse searching time increase, but also a longer pulse is generally more susceptible for decoherence effect.

4.3.2 Control Technique 1: Gradient Ascent Pulse Engineering (GRAPE)

In order to implement the complicated pulses, the GRAPE algorithm was developed [14]. Most of the pulses used in this experiment were found using the GRAPE algorithm. The GRAPE algorithm is a numerical optimization technique to search for high-fidelity control pulses. The algorithm considers the full Hamiltonian written in Equation 4.20 and outputs the ω_{nut} and ϕ which optimizes the fidelity,

$$F = \frac{|\text{Tr}(U_{\text{goal}}^{\dagger}U_{\text{sim}})|^2}{D^2} \tag{4.21}$$

where U_{goal} is a desired unitary and U_{sim} is the simulated unitary using the GRAPE algorithm. Here, U_{sim} is discretized into N equal time steps of length Δt during which the external Hamil-

tonian is constant,

$$U_{\text{sim}} = \prod_{k=1}^{N\Delta t} e^{-i(\tilde{H}_{\text{nat}}+\omega_{\text{nut}}^{k}[\cos(\phi_p^k)\sum_i X_i+\sin(\phi_p^k)\sum_i Y_i])\Delta t}, \tag{4.22}$$

where N is the number of time steps. The pulse duration τ is NΔt. The details of how the algorithm achieves optimization can be found in [14, 34]. In the GRAPE algorithm, one can also search for a pulse robust to rf-inhomogeneity and fluctuations in the Larmor frequency. However, this requires a longer time for optimization, since the algorithm needs to sweep through the distributions of rf-inhomogeneity and Larmor frequencies to ensure the robustness of the pulse at those conditions. Typically, for liquid-state NMR experiments, a pulse is optimized for rf-inhomogeneity, but not fluctuations of Lamor frequencies. One thing to note is that it is hard to know whether the minimum found by GRAPE is the global minimum or a local minimum. For instance, varying the initial conditions of the search typically results in different optimized pulses, and in a few cases, one might not be able to find a high-fidelity pulse if an initial guess is not appropriate[2].

The pulse that prepares the ground state of the 7-qubit Kitaev's Lattice Model (Figure 4.4 a) was found using GRAPE with Δt=10μs and $N = 6000$ (Figure 4.4 b). The pulse time is the one of the inputs that need to be specified, and it can be usually estimated by looking at how many single-qubit or two-qubit gates are in the desired circuit. For our sample, a single-qubit case typically takes 1ms and a two-qubit case takes 20ms (J-coupling evolution between the carbons). Also, the pulse was optimized for rf-inhomogeneity as well [3]. One of the steps that dominates the computing time is exponentiating the matrix. Thus, to reduce the computing time by starting with an initial guess close to a desired unitary, we use the subsystem approach: partition the system into two subsystems and search for a high-fidelity pulse, then use this high-fidelity output as the initial guess for the algorithm using the full Hamiltonian of the system.

The following settings for some of the inputs to the GRAPE algorithm written in MATLAB [34] were used for the all the GRAPE pulses found for this experiment.

params.rfdist=[0.3,0.97; 0.4 1.00; 0.3 1.03];
=¿ to make a GRAPE pulse robust to rf-inhomogeneity. With this setting, the algorithm finds the pulse which is robust to the defined rf-inhomogeneity profile of 30% spins experiencing 97%

[2]It happened once that Dawei could not find a high-fidelity rotation pulse on C6 (a 12-qubit pulse, no decoupling), thus, he ran the algorithm many times with random initial guess and finally found one].

[3]It took about 5 days to find the pulse with 99% fidelity using the ordi2 server

of the rf power, 40% spins 100% of the power, and the last 30% 103%. Although it seems like a very narrow distribution, the pulse optimized with such a distribution performs much better experimentally than optimized ones[4].

params.Hdist=[1];
=¿ to make a GRAPE pulse robust to natural Hamiltonian variations. Variations are usually caused by drifting of ω_i parameters depending on various experimental conditions, i.e. temperature, humidity etc). For our purposes, we assumed that there are no variations to reduce the time to find a high fidelity pulse. Thus, the GRAPE pulses used in this experiment are not designed to be robust to variations in the natural Hamiltonian.

params.softpulsebuffer=4e-6;
=¿ an output unitary pulse includes -4us free evolution before and after a target unitary (i.e. $U_{\text{target}} = U_{\text{free}}(-4\mu s)U_{\text{want}}U^{\dagger}_{\text{free}(-4\mu s)}$) to cancel out the necessary 4μs buffer delay time before and after the pulse in the spectrometer setting. The default time delay required in the spectrometer to apply the soft pulse is 4μs.

For the 7-qubit pulses: **params.subsystem**{**1**}=[1 2 3 4 5 6 7];
For the 12-qubit pulses: **params.subsystem**{**1**}=[1 2 3 9 10 11];
params.subsystem{**2**}=[4 5 6 7 8 12];
=¿ for the 12-qubit pulses, the sub-system approach (assuming that there is no interaction between the two subsystems) was used to reduce the search time. Subsequently, the fidelity is recalculated using the full Hamiltonian.

[4]this was one of the key step which improved our data

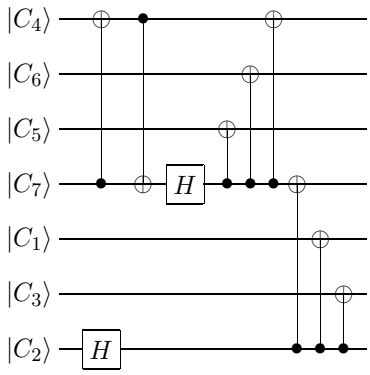

(a) GD Gate

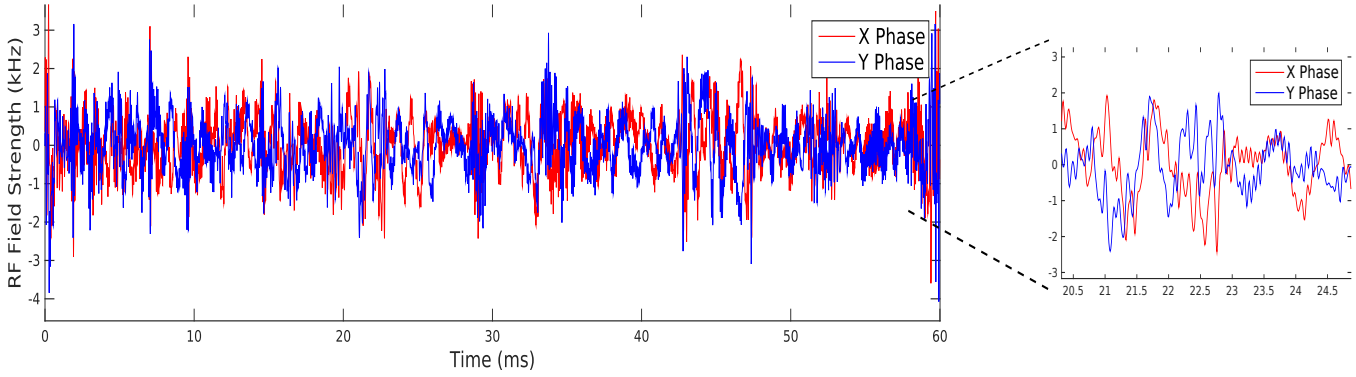

(b) GD Pulse

Figure 4.4: Implementation of the ground state preparation circuit using the GRAPE algorithm: (a) the circuit being implemented using the GRAPE (b) the real and imaginary parts, which can be translated into the amplitudes and phases, of the output 99% fidelity pulse produced by the GRAPE algorithm with $\Delta t = 10\mu s$ and $N = 6000$.

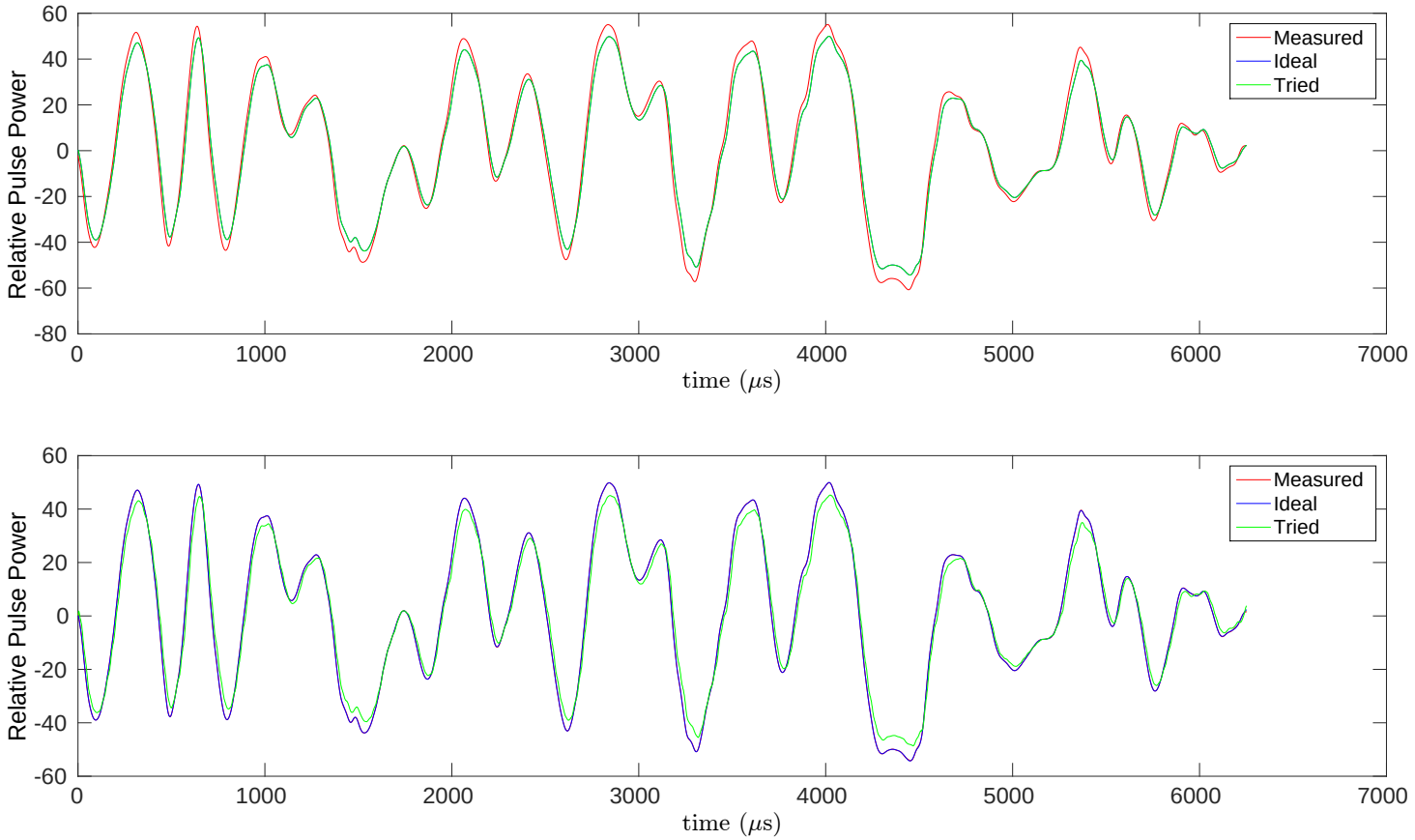

Figure 4.5: RF selection pulse generated using the GRAPE algorithm without (top) and with (bottom) pulse fixing. 'Ideal', 'tried', 'measured' pulse shapes are the desired pulse shape, actual pulse generated by the spectrometer, and the field field picked up at the sample position via a small pick-up coil. In the figure before pulse fixing, 'Tried' and 'Ideal' pulse shapes overlap as expected. After going through the iterative feedback algorithm which adjusts the 'tried' pulse, the 'measured' pulse shape and 'ideal' pulse shape match better.

4.3.3 Control Technique 2: Pulse-Fixing

To achieve a high-fidelity control of NMR systems for quantum information purposes, unconventional complicated pulses, especially those generated by the GRAPE algorithm, need to be implemented with a high precision. Although commercial NMR spectrometers are equipped with relatively precise instruments, non-linearities in the pulse generation and amplification can still cause large discrepancies between the ideal rf fields to be implemented and the actual rf fields that the spins in the sample receive [34]. These discrepancies are especially predominant for complex pulse shapes.

To fix such discrepancies, the field at the sample position is measured through a small pick-up coil and the applied control rf pulses are adjusted iteratively through a feedback loop until the field at the sample matches the desired pulse.

4.3.4 Control Technique 3: RF selection

The rf-inhomogeneities (small variations in the rf magnetic field), arise from reasons such as coil geometries and sample imperfections. This leads to variations in the ω_{nut} within the sample. Thus, spins at different physical locations experience slightly different rf power than desired. Therefore, this effect leads to pulse imperfection.

The rf selection method is used to circumvent such pulse imperfection by selecting those spins at locations where the rf field is homogeneous, typically chosen to be in range 97 to 103% of the desired rf power. There are two methods: the method used in [18] which uses a sequence of $\pi/2$ and π rotations along various axes; and a GRAPE pulse [34]. In both methods, the spins outside of the desired rf-homogeneity range end up in an X or Y state (assuming the case of a single qubit system), whereas the spins within the range stay as Z or $-Z$. Then, by applying magnetic gradient fields, the signal from the spins outside of the range averages out, leaving only the 'good' spins.

We used the GRAPE pulse to implement the rf selection [5]. This pulse has been used by the group previously. The pulse was found assuming that the natural Hamiltonian is zero (one qubit system with the resonance at its Larmor frequency). However, this pulse works surprisingly well for multi-qubit systems such as crotonic acid and dichloro-cyclobutanone. We simulated the

[5] I also tried using the method used in [18], but it was harder to pulse-fix such sequence than the GRAPE pulse

GRAPE rf selection pulse on the dichloro-cyclobutanone sample in state $IIIIIIZ_{C_7}$ to check the performance of the rf selection pulse on dichloro-cyclobutanone. In the simulation, the pulse is on resonance with the Larmor frequency of C_7, and the inhomogeneity factor ϵ is added at every time step of the external Hamiltonian

$$U_{\text{rfsel}} = \prod_{k=1}^{N\Delta t} e^{-i(\tilde{H}_{\text{nat}}+(1+\epsilon)\omega_{\text{nut}}^k[\cos(\phi_p^k)\sum_i X_i+\sin(\phi_p^k)\sum_i Y_i])\Delta t}, \tag{4.23}$$

where ω_{nut}^k and ϕ_p^k are the amplitudes and phases of rf selection pulse. Subsequently, the gradient effect was simulated to dephase the signal from the inhomogeneous spins. Figure 4.6 shows the fidelity (Equation 4.24) between the output state and Z_{C_7}, which is the state when ϵ=0, with respect to the inhomogeneity factor ϵ.

$$F = \frac{|\text{Tr}(\widetilde{\rho}_{\text{rfsel}}(-Z_{C_7}))|}{128} \tag{4.24}$$

where $\widetilde{\rho}_{\text{rfsel}}$ is the simulated output state. Furthermore, we analyzed the simulated output state at $\epsilon = 0$ to examine the unwanted Pauli components by decomposing the state into product operator basis. The analysis showed that the largest Pauli components after Z_{C_7} are $X_{C_4}X_{C_7}$, $X_{C_4}Y_{C_7}$, $Y_{C_4}X_{C_7}$, and $Y_{C_4}Y_{C_7}$, contributing about 10% compared to Z_{C_7} component:

$$\widetilde{\rho}_{\text{rfsel}} \propto Z_{C_7} + 0.0914X_{C_4}Y_{C_7} - 0.0733X_{C_4}Y_{C_7} + 0.0733Y_{C_4}X_{C_7} + 0.0914Y_{C_4}Y_{C_7} \tag{4.25}$$

We experimentally observed that after rf-selection the contributions from C_4 and C_7 interactions are apparent. Therefore, it is necessary to remove these contributions by rotating C_1 to C_6 around both x- and y-axis followed by the magnetic gradient. Also, to check whether the rf-selection worked experimentally, we rotated the spins through many 2π rotations to ensure that the rf-selection step indeed reduced the effect from field-inhomogeneities.

4.3.5 Decouple (Waltz 16)

It is necessary to remove the spin-spin couplings between the carbon and hydrogen atoms to obtain the effective 7-qubit system of carbon atoms. The coupling causes the transitions of a

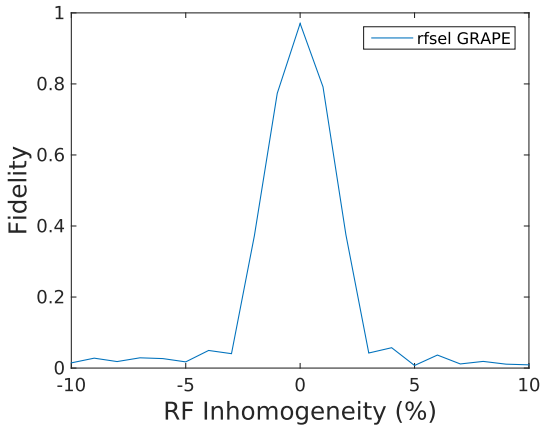

Figure 4.6: The simulated fidelity (Equation 4.24) of the state Z_{C_7} after the rf-selection pulse followed by the magnetic gradient on the decoupled dichloro-cyclobutanone sample. It shows that the rf selection pulse selects those spins lying within $1\pm \sim 3\%$ of the rf-homogeneity.

spin which depend on the states of the other coupled spins. These transitions of the spin mediated by the couplings occur in a lifetime larger than inverse of the coupling strength, $1/J$. The basic idea behind a decoupling method is to shorten the lifetime of the other coupled spins to be much shorter than $1/J$. In this way, the transitions due to the coupling will not be observed.

There are two main ways to achieve decoupling: selective and is broad-band decoupling. A selective decoupling is accomplished by a very long pulse centered at the Larmor frequency of the spin of interest. A broad-band decoupling (or composition pulse decoupling, cpd) is achieved by exciting a large frequency range using a sequence of short pulses applied in rapid succession. Since we are decoupling all hydrogen atoms (a frequency range of 2kHz), we use a broad-band method.

The rapid series of pulses causes fast transitions of hydrogen atoms such that the lifetime of any particular hydrogen spin in any given state is shorter than $1/J$ (here, J is the typical coupling strength of carbon and hydrogen spins on the order of $\sim$100Hz). The particular broad-band decoupling sequence used in this experiment is Waltz-16, which is shown in Figure 4.7. The pulse length of the short pulses in the sequence is on the order of μs, whereas the coupling lifetime is in order of ms. Thus, the effect of decoupling is almost instantaneous.

One caution to note is that the Waltz-16 is known to induce the magnetization transfer between

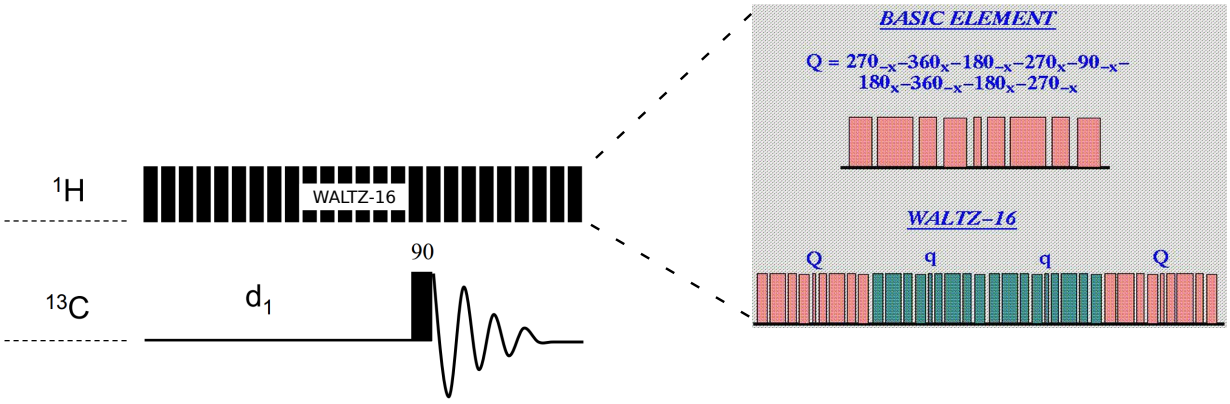

Figure 4.7: A broad-band decoupling scheme using a Waltz-16 sequence: hydrogen atoms are irradiated with a train of short square pulses as shown in the figure (the figure shows only a single hydrogen spin, but for our case, the short pulse acts on a frequency range of H_1 to H_5). It is important to note that hydrogen atoms are irradiated during the acquisition of FID as well. A sequence shown on the right, Waltz-16, rapidly changes the state of hydrogen spins such that the transition of carbon spins due to the coupling to hydrogen spins are neglected. In the sequence Q, θ_{axis} represents a rotation of a spin by θ along the specified axis. Moreover, q is an inverted sequence of Q (i.e. the axis of rotation is inverted by 180 degree, 270_{-x} to 270_x). The figures on the left and right are adopted from [38] and [30], respectively.

the coupled spins through the Nuclear Overhauser Effect (NOE) [2, 32]. Therefore, it is necessary to experimentally check that such a process does not interfere significantly to this experiment.

4.3.6 Polarization swap between C7 and H5

Since a hydrogen atom has a higher polarization than a carbon atom, $\gamma_{\text{H}}/\gamma_{\text{C}} \approx 3.98$, we swap the polarization of C7 and H5 to increase the signal of C7. Thus, we can achieve a better signal-to-noise (SNR) ratio given a fixed number of scans.

The 12-qubit swap pulse was found using the GRAPE algorithm. This pulse takes the state $\sum_{i=1}^{5} Z_{\text{H}_i}$ to $\sum_{i=1}^{4} Z_{\text{H}_i} + Z_{\text{C7}}$.

Chapter 5

NMR Implementation

The following section outlines an NMR implementation of the theoretical proposal introduced in Chapter 3, using the techniques discussed in Chapter 4.

5.1 Experimental Overview

The NMR implementation of the anyonic experiment is divided into five main steps (Figure 5.1).

1. State Preparation ($\sim$ 100ms): preparation of $\widetilde{\rho}_{\text{PPS}} = |000000\rangle\langle 000000| Z_{\text{C}_7}$ from the thermal state.
2. Ground State Preparation (60ms): preparation of the ground state of the 7-qubit Kitaev's Lattice Model.
3. Anyonic Creation, Braiding and Annihilation (1ms)
4. Measurement (60ms): changes the basis of the state such that the anyonic phase can be estimated from the populations of a density matrix.
5. Read-out (1ms): rotates C_7, generating the the single-coherence terms from the populations which induces the NMR signal, to measure $|\alpha|^2$ and $|\beta|^2$ from which θ_{anyon} can be estimated.

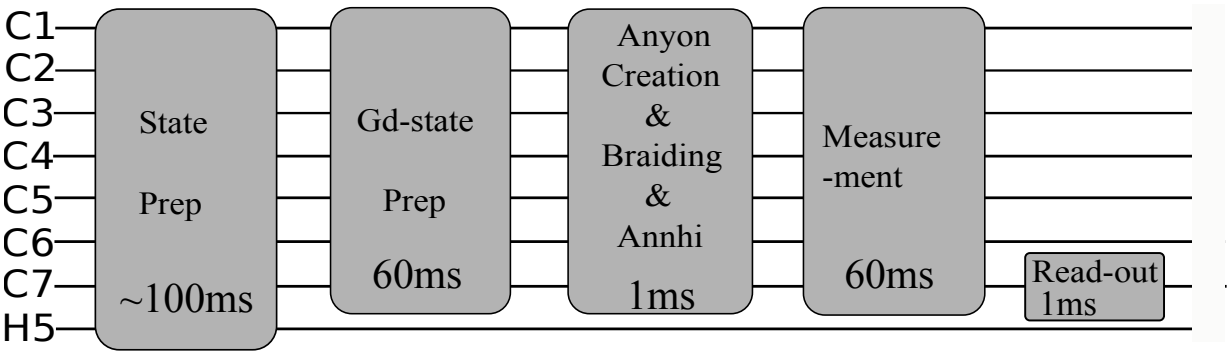

Figure 5.1: The schematic NMR circuit showing the overview of the experimental scheme: the state preparation ('State Prep') to generate the initial labelled PPS state $|000000\rangle\langle 000000| Z_{C_7}$, the ground state preparation step, anyon manipulation step which includes creation, braiding, and annhilation of anyons, measurement step to change the basis of the state and lastly, the read-out pulse rotating C_7 is applied to measure the state, which is deciphered by observing the C_7 spectrum.

5.1.1 State Preparation

The state preparation step consists of five steps as shown in Figure 5.2.

a. Polarization Crusher: the goal of this step is to take the thermal state $\widetilde{\rho} = \sum_i^{i=7} Z_{C_i} + 4\sum_i^{i=5} Z_{H_i}$ to $4\sum_i^{i=5} Z_{H_i}$, leaving only the hydrogen polarizations (the hydrogen polarization is ~4 times larger than the carbon polarization). This can be achieved by rotating all carbon spins to $\sum_i^{i=7} X_{C_i}$ and applying magnetic gradient.

b. State exchange (SWAP[1]) between C_7 and H_5 (Section 4.3.6): take the state $4\sum_i^{i=5} Z_{H_i}$ to $4Z_{C_7} + 4\sum_i^{i=4} Z_{H_i}$, boosting the polarization of C_7.

c. Decouple (Sequence Name: Waltz 16) (Section 4.3.5): start decoupling the carbon and hydrogen spins. This stays turned on for the duration of the experiment.

d. RF selection on C_7 (Section 4.3.4): applying the rf-selection pulse on resonance to C_7 followed by the magnetic gradient.

e. Labelled Pseudo-Pure State Preparation (Section 4.2): create the initial state $|000000\rangle\langle 000000| Z_{C_7}$.

[1]Although we refer this step as SWAP, the pulse does not implement the SWAP gate. The pulse implements 2 CNOT gates, rather than 3 which is the case of the SWAP gate.

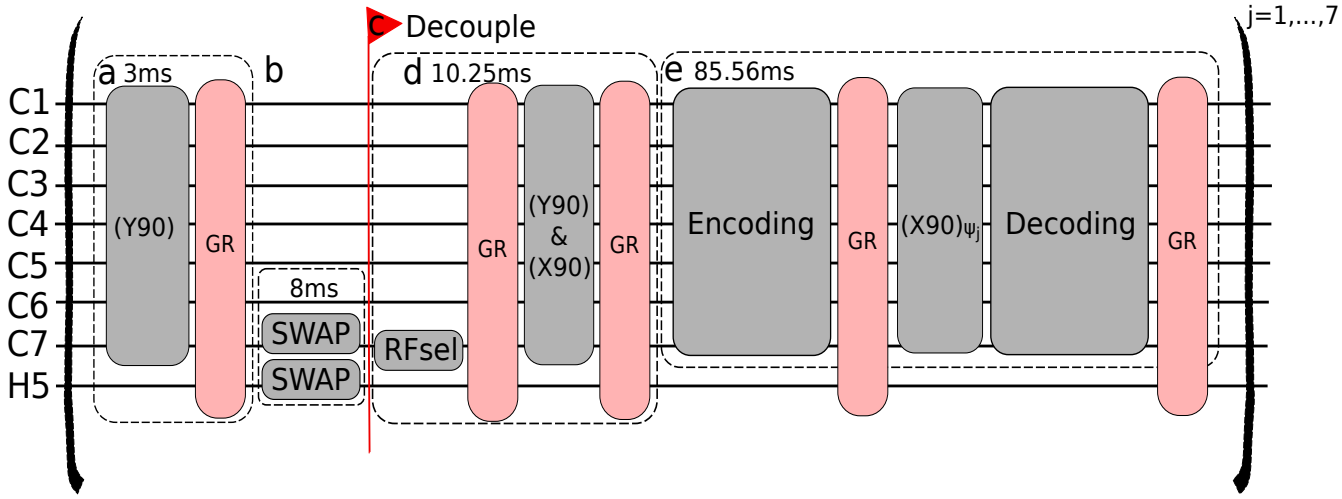

Figure 5.2: The NMR circuit of state preparation step: a) polarization crusher step which takes the thermal state $\sum_i^{i=7} Z_{C_i} + 4\sum_i^{i=5} Z_{H_i}$ to $4\sum_i^{i=5} Z_{H_i}$ which is done by rotating all the carbon spins by 90° along y-axis (Y90) followed by magnetic gradient (GR) b) boosts the polarization of C_7 by exchanging the state of C_7 and H_5 (SWAP) c) start decoupling the carbon and hydrogen spins and it stays turned d) RF selection targeted on C_7 e) labelled PPS preparation. The above steps are repeated for 7 times with different phases of ψ_j to select the appropriate coherence [phase cycling for the step (e)]. For simplicity, the rest of hydrogen spins are not shown in the figure.

5.1.2 Ground State Preparation

Figure 5.3 (a) shows the circuit that prepares the ground state. The high-fidelity pulse which implements such a circuit was found using the GRAPE algorithm (Section 4.3.2). Unlike the theoretical proposal discussed in Chapter 3, the NMR implemented circuit prepares the ground state from the mixed deviation matrix $|000000\rangle\langle 000000| Z_{C_7}$ rather than the pure state $|0000000\rangle$. Therefore, the state after the ground state pulse is:

$$\widetilde{\rho}_{\text{gd\_exp}} = \frac{1}{2}\left(|\psi_{\text{ground}}\rangle\langle\psi_{\text{ground}}| - \left|\psi'_{\text{ground}}\right\rangle\left\langle\psi'_{\text{ground}}\right| \right) \tag{5.1}$$

where $\left|\psi'_{\text{ground}}\right\rangle$ results from the part $|0000001_{C_7}\rangle$ of the initial state $|000000\rangle\langle 000000| Z_{C_7}$. In theory, this extra state does not interfere with the subspace of $|\psi_{\text{ground}}\rangle$ throughout our experimental scheme. The additional two CNOT gates in the ground state preparation circuit in Figure 5.3 (a) compared to the theoretical circuit (Figure 3.2) were specifically added to achieve this. Therefore, it is reasonable to neglect the signal from the additional state throughout the experiment.

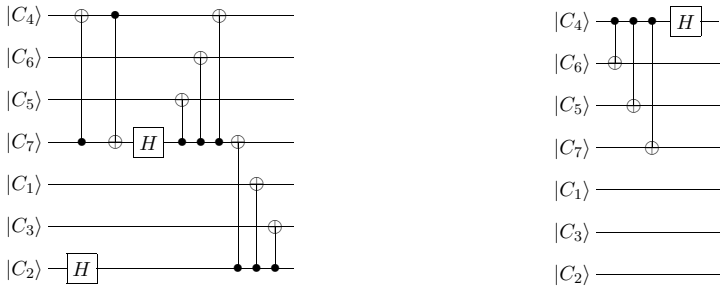

(a) GD (b) MM

Figure 5.3: The quantum circuits of (a) the ground state preparation and (b) measurement step [change of basis step after anyonic manipulation]. The GRAPE algorithms were used to find the high-fidelity pulses that implement the above gates.

5.1.3 Anyon Creation, Manipulation and Annihilation

To optimize the circuit, anyon creation, manipulation and annihilation steps are compressed into single qubit rotations as shown in Figure 5.4. In the figure, BD0, BD1, and BD2 denote the gates implementing the trivial braiding loop ($X_4X_5X_6X_7$[2]), the first non-trivial braiding loop ($X_7X_6X_3X_1X_2X_5$), and the second non-trivial braiding loop ($X_4X_3X_2X_1$), respectively. Refer to Figure 3.1 for the possible braiding loops in the 7-qubit Kitaev's Lattice Model. Again, the pulses implementing the braiding gates were found using the GRAPE algorithm.

5.1.4 Measurement

Figure 5.3 (b) shows the circuit that implements the measurement step. The GRAPE algorithm is used to find the high-fidelity pulse which implements such a circuit. The theoretical final state after the measurement pulse is

$$\begin{aligned}\widetilde{\rho}_{e\_\text{exp}} =& \frac{1}{2}\left(|\psi_{\text{mm}}\rangle\langle\psi_{\text{mm}}| - \left|\psi'_{\text{mm}}\right\rangle\left\langle\psi'_{\text{mm}}\right|\right) \\ =& \frac{1}{2}\left(|\alpha|^2|\psi_{\text{p0}}\rangle\langle\psi_{\text{p0}}| + \alpha\beta^*|\psi_{\text{p0}}\rangle\langle\psi_{\text{p1}}| + \alpha^*\beta|\psi_{\text{p1}}\rangle\langle\psi_{\text{p0}}| + |\beta|^2|\psi_{\text{p1}}\rangle\langle\psi_{\text{p1}}| - \left|\psi'_{\text{mm}}\right\rangle\left\langle\psi'_{\text{mm}}\right|\right),\end{aligned} \tag{5.2}$$

[2]The order of numbering is in the qubit numbering (Figure 3.2), not carbons.

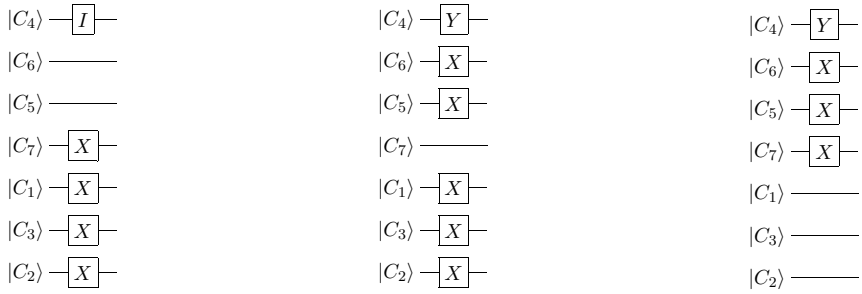

(a) BD0 (b) BD1 (c) BD2

Figure 5.4: The anyonic manipulation gates with anyon creation, braiding, and annihilation compressed into single qubit rotations: BD0 implements trivial loop ($X_4X_5X_6X_7$), BD1 implements the first non-trivial loop ($X_7X_6X_3X_1X_2X_5$), and BD2 implements the second non-trivial loop ($X_4X_3X_2X_1$) [Figure 3.1].

where $|\psi_{\text{mm}}\rangle = \alpha\,|\psi_{\text{p0}}\rangle + \beta\,|\psi_{\text{p1}}\rangle$ with $|\psi_{\text{p0}}\rangle = |0000000\rangle + |0001111\rangle$ and $|\psi_{\text{p1}}\rangle = |1000000\rangle + |1001111\rangle$, and $\left|\psi'_{\text{mm}}\right\rangle\left\langle\psi'_{\text{mm}}\right|$ is the state resulting from the $|000001_{\text{C}_7}\rangle$ part of the initial state $|000000\rangle\langle 000000|\,Z_{\text{C}_7}$ which we neglect. Recall that $\theta_{\text{anyon}} = 2\arctan(\sqrt{|\beta|^2/|\alpha|^2}\,)$ as mentioned in Equation 3.8.

5.1.5 Read-out

The read-out pulse rotates C_7 by $\pi/2$ around the y-axis. The pulse was found using GRAPE. This read-out pulse generates the single coherences from the populations. Specifically, for estimating $|\alpha|^2$ and $|\beta|^2$ from $\widetilde{\rho}_{e\_\text{exp}}$, it generates the below single coherences up to a constant:

1. $|0000000\rangle\langle 0000000| \xrightarrow{R_y(\pi/2)_{\text{C}_7}} |0001000\rangle\langle 0000000| + \ldots$
2. $|0001111\rangle\langle 0001111| \xrightarrow{R_y(\pi/2)_{\text{C}_7}} |0000111\rangle\langle 0001111| + \ldots$
3. $|1000000\rangle\langle 1000000| \xrightarrow{R_y(\pi/2)_{\text{C}_7}} |1000000\rangle\langle 1001000| + \ldots$
4. $|1001111\rangle\langle 1001111| \xrightarrow{R_y(\pi/2)_{\text{C}_7}} |1000111\rangle\langle 1001111| + \ldots,$

which produces the NMR peaks at distinct frequencies of C_7 spectrum. The $|\alpha|^2$ and $|\beta|^2$ are estimated by determining the coefficients (which can be translated into magnitude and phase) of the relevant peaks.

5.2 GRAPE Pulses

Table 5.1 lists the pulses used in the experiment.

Bruker Pulse Name	**Unitary Name (.mat file)**	**Unitary**	**Duration** τ (μs)	dt (μs)	**Fidelity**
twqubit_sub_C1toC790_C_12500 twqubit_sub_C1toC790_H_12500	U_twqubit_C1toC790	$Y(90)_{H_1} Y(90)_{H_2} Y(90)_{H_3} Y(90)_{H_4}$- $Y(90)_{H_5} Y(90)_{C_1} Y(90)_{C_2} Y(90)_{C_3}$- $Y(90)_{C_4} Y(90)_{C_5} Y(90)_{C_6} Y(90)_{C_7}$	1000	10	0.9969
twqubitsub_swapC7H5_8ms_C_12500 twqubitsub_swapC7H5_8ms_H_12500	U_full_8ms_swap	(state to state) $4\sum_{i=1}^{5} Z_{H_i} \rightarrow 4\sum_{i=1}^{4} Z_{H_i} + 4C_7$	8000	10	0.9936
rfsel4	rfsel()	Section 4.3.4	6250	10	0.9702
Unitary_C1toC6rot_125kHz	U_full_C1toC6rot	$Y(90)_1 Y(90)_2 Y(90)_3 Y(90)_4$- $Y(90)_5 Y(90)_6$	1000	10	0.9900
enc_F99_125kHz	enc_F99	(state to state) $Z_7 \rightarrow$ ZZZZZZZ	42280	10	0.9967
Unitary_C1toC7rot_125kHz	U_full_C1toC7rot	$Y(90)_1 Y(90)_2 Y(90)_3 Y(90)_4$- $Y(90)_5 Y(90)_6 Y(90)_7$	1000	10	0.9902
dec_F99_125kHz	dec_F99	(state to state) 7 coherences $\rightarrow 000000 Z_7$	42280	10	0.9916
U_ground_125kHz_F99	sevenbit_gd_F99	Figure 4.4 (a)	60000	10	0.9930
U_stab1_125kHz	U_stab1_full	$Y(90)_7$	1000	10	0.9951
U_stab2_125kHz	U_stab2_full	$X(90)_4 Y(-90)_5 X(90)_6$	1000	10	0.9945
U_stab3_125kHz	U_stab3_full	$X(90)_4 X(90)_5 Y(-90)_6$	1000	10	0.9947
U_stab4_125kHz	U_stab4_full	$X(90)_4 Y(-90)_5 Y(-90)_6$	1000	10	0.9944
U_stab5_125kHz	U_stab5_full	$Y(-90)_1 X(90)_2 Y(-90)_3$- $X(90)_4 Y(-90)_5 Y(-90)_6 Y(90)_7$	1000	10	0.9949
braiding0_F99_125kHz_updated	U_bd0_grape_updated	$X_7 X_1 X_3 X_2$	1000	5	0.9946
braiding_F99_125kHz	U_bd_grape_updated	$Y_4 X_6 X_5 X_1 X_3 X_2$	1000	5	0.9959
braiding2_F99_125kHz	U_bd2_grape_updated	$Y_4 X_6 X_5 X_7$	1000	5	0.9965
mm_F99_125kHz	mm_F99	H_7CNOT(4,7)CNOT(4,6)CNOT(4,5)	60000	5	0.9909

Table 5.1: Pulses used in the experiment

5.2.1 GRAPE Pulses on Thermal State

To check the performance of each pulse, the pulse-fixed GRAPE pulses were tested on the thermal state and compared to the simulated spectra (numerical simulation of the GRAPE pulse on the thermal state). We found several GRAPE pulses that implement the same unitaries, and through such a test, we chose the one that performs better experimentally (the one that gives more similar spectra to the simulated spectrum).

5.3 Experimental Protocol

1. Lock the signal to acetone-d6 for the Dichloro-cyclobutanone sample.
2. Tune and Match the probe.
3. Shim B_0
   (a) Use Bruker Topspin commands 'rsh' and 'wsh' to load the previous shim values and save the current shim values, respectively.
4. RF Pulse Calibration
   (a) calibrate 12.5kHz and 25kHz of carbon pulsing channel (F3) by applying a hard pulse on C1 (Section 5.3.1).
   Pulse and au program used: 'zg_freqlist_f3' and 'au_test4_annie'.
   Parameters: $cnst0$=9324, $p1$=80μs (for 12.5kHz) and 60μs (for 25kHz), and scan $pl3$ from 1.5 to 2.0 (for 12.5kHz) and -4.5 to -4.0 (for 25kHz).
   (b) calibrate a $\pi/2$ pulse of carbon pulsing channel (F3).
   Pulse program: 'zg_calib90'
   Parameters: $cnst0$=9324, set $pl3$ to the 12.5kHz calibration value, scan $p1$ from 20μs to 23μs.
   (c) calibrate 12.5kHz of hydrogen pulsing channel (F2)
   Pulse program:'zg_calib90_H'
   Parameters: $p1$ to calibrated value from the above, p2=60μs, $pl3$ to the calibrated from the first step, and scan $pl2$ from 11.8 to 12.4.
5. Take the sample out, and pulse-fix using the calibrated power.

6. Put the sample back and repeat steps 1-3. Run the pulse sequence implementing the circuit shown in Figure 5.1 and check the state inbetween the circuit. As the RF selection pulse is sensitive to the power level, the power of the RF pulse should be swept from -4.2 to -4.6dB. After the RF-selection, the power level should be re-calibrated. Typically, dB increases by $\sim$0.3dB.

5.3.1 RF Pulse Calibration

Basics

To achieve the high-fidelity control of a quantum system using NMR, it is important to apply the desired amplitude of the oscillating B_1 field. In the spectrometer, the transmitter power of the pulse generator is specified in decibels (dB) of attenuation. Therefore, an appropriate unit conversion is necessary to know which value of dB corresponds to the desired B_1 field. The two units are related through the following relationship below,

$$dB_j - dB_i = 20\ log\left(\frac{V_i}{V_j}\right) = 20\ log\left(\frac{B_{1i}}{B_{1j}}\right) \tag{5.3}$$

where V and B_1 denote the voltage and strength of B_1 fields in Hz respectively. Thus, lowering dB corresponds to increasing B_1. For example, decrease in power by 6dB requires increasing B_1 by a factor of 2.

However, since Equation 5.3 only provides the relative relationship between two power values, it is necessary to find the reference power value. We calibrate this reference power by finding when a given pulse achieve a 2π rotation, as is conventional. A hard pulse (a rectangular pulse) of a pulse length τ_p and a field strength B_1 rotates the spin on resonance to a flip angle,

$$\Theta = \gamma B_1 \tau_p = 2\pi B_{nut} \tau_p \tag{5.4}$$

where B_{nut} is a nutation frequency γB_1 in Hz. To get a 2π rotation at a desired nutation frequency B_{nut}, a pulse length τ_p should be set to $1/B_{nut}$. Starting with a low power, we increase the power level at an appropriate rate to find the dB value which achieves a 2π rotation. This specific dB value corresponds to the desired B_{nut} and can be used as the reference. Note that a 2π rotation occurs at the second zero crossing, not the first at π.

Technical Detail related to Calibration

For both of the carbon and hydrogen channels, we calibrated for the reference power levels of 25kHz and 12.5kHz according to the method mentioned previously. Before starting a calibration step, it is important to decide on the channel map (i.e. the connection of a virtual logical channel to a physical Signal Generation Unit (SGU) and amplifer), since the calibration is different depending on which SGU unit is used. The channel map can be specified with a topspin command 'edasp'. Figure 5.5 shows the channel map used for this experiment. Table 5.2 shows the typical values of the calibration.

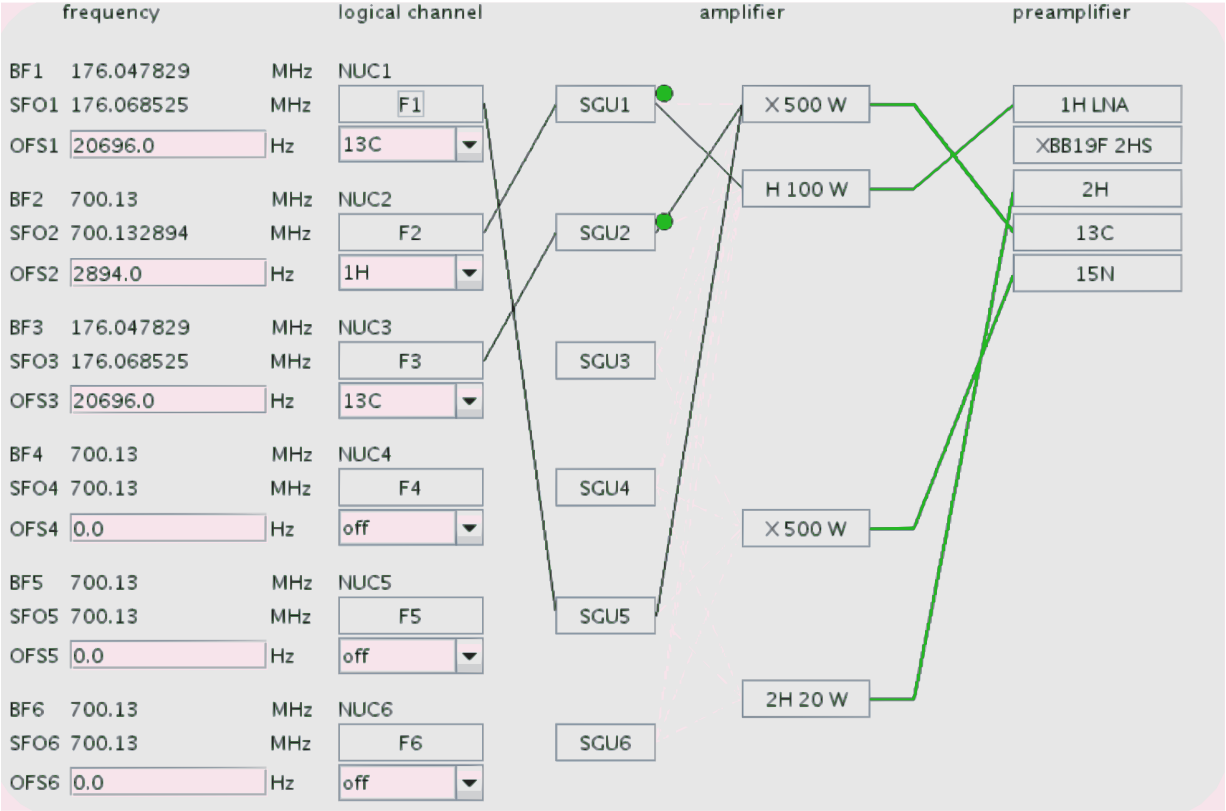

Figure 5.5: The channel map used for the experiment. The calibration of the channels depend on the channel map. Thus, it is important to keep the channel map consistent through out the experiment. F1 is the observation channel which specifies which nucleus we are observing, and F2 and F3 are the pulsing channels.

Sample & Channel	B_{nut}	dB
12-q sample, C	25kHz	∼-4.50
12-q sample, C	12.5kHz	∼1.75
12-q sample, H	25.0kHz	∼6.2
12-q sample, H	12.5kHz	∼12.15

Table 5.2: Calibration values with the specificed channel map shown in Figure 5.5

Calibrating the power of F2: The calibrated powers of F2 (a logical channel 2) change if the observation nucleus of the observation channel (F1) changes from carbon to hydrogen, which suggests that there might be some crosstalk between SGUs. We observed ∼1dB difference in the power level of F2 when the observation nucleus of F1 was set to carbon and hydrogen. What this means is that the rf power on hydrogen (power level of F2) needs to be calibrated by observing carbon with our channel map setting (Figure 5.5) (since we are interested in observing carbon). Below is a three-qubit example of how to achieve such calibration.

$$Z_{\mathrm{C}} I_{\mathrm{H}} I_i \xrightarrow{\text{step 1: } \pi/2 \text{ rotation on C}} Y_{\mathrm{C}} I_{\mathrm{H}} I_i \tag{5.5}$$

$$\xrightarrow{\text{step 2: ZZ evolution for } t=1/2J_{\mathrm{CH}}} X_{\mathrm{C}} Z_{\mathrm{H}} I_i \cos(\phi) + Y_{\mathrm{C}} Z_{\mathrm{H}} Z_i \sin(\phi) \tag{5.6}$$

$$\xrightarrow{\text{step 3: apply } U=e^{-i\omega_{\mathrm{nut}} Y_{\mathrm{H}} t/2}} X_{\mathrm{C}} Z_{\mathrm{H}} I_i \cos(\phi)\cos(\omega_{\mathrm{nut}} t) + X_{\mathrm{C}} X_{\mathrm{H}} I_i \cos(\phi)\sin(\omega_{\mathrm{nut}} t) \tag{5.7}$$

$$+ Y_{\mathrm{C}} Z_{\mathrm{H}} Z_i \sin(\phi)\cos(\omega_{\mathrm{nut}} t) + Y_{\mathrm{C}} X_{\mathrm{H}} I_i \sin(\phi)\sin(\omega_{\mathrm{nut}} t) \tag{5.8}$$

In the above example, I considered the three spins of one carbon, one hydrogen, and additional of C or H spin, which have J-couplings to each other. After step 2 of ZZ evolution, ϕ indicates the evolution of $Z_C Z_i$ which depends on J_{Ci}. If the pulse applied on H is a perfect $\pi/2$ pulse, no signal will be observed on C spectrum. Thus, it is possible to calibrate the rf power on H by finding the dB which achieves this point. In our experiment, we find when the $3\pi/2$ rotation happens using C_4 and H_1 (for the same reason described above for finding 2π rotation instead of $\pi/2$).

5.3.2 Other Experimental Detail

The details of the pulse-fixing feedback algorithm and the experimental protocol can be found in [34]. In this sub-section, I will write about parts that are not discussed in those documents.

Generating Bruker Pulse Shape Format: After generating a GRAPE pulse, the amplitudes and

phases of the pulse at each time step need to be re-written in the file format that the spectrometer can comprehend. We refer to this file format as a 'Bruker Shape Format'. In this file format, the amplitudes of a pulse are written as a percentage of the reference power. One thing to note is that this reference power should be the largest power. What this means is that the amplitudes of a pulse written in 'Bruker Shape Format' should not exceed 100%. A SGU unit generates up to 100% of the reference power regardless of the strength of the amplitude: i.e. it will only generate 100% even at amplitudes which exceed 100%. Figure 5.6 shows the measured signal at the sample position when a linear pulse from 1% to 150% is implemented. The response above the 100% results in a flat line. For the pulses used in this experiment, the reference amplitudes were either fixed to 12.5kHz or 25kHz, since the corresponding attenuation values (dB) are known through the calibration step [Section 5.3.1] Note for a spectrometer to implement a pulse, the reference amplitudes need to be specified in dB.

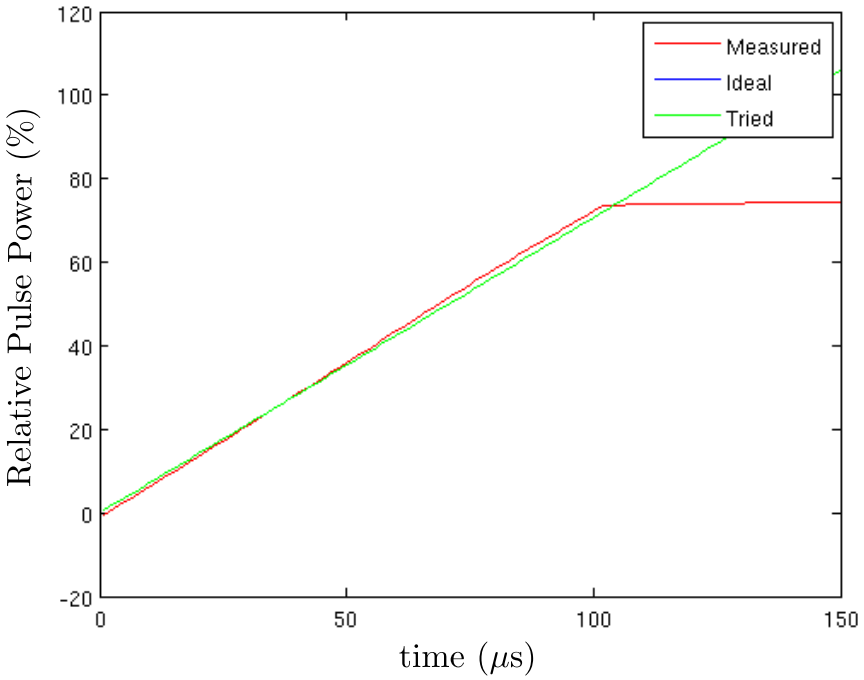

Figure 5.6: The signal measured by the pick up coil (red line) when the linear pulse from 1% to 150% of a specified maximum power (green line) is implemented. A SGU unit generates only up to 100% of the reference power regardless of the strength of the reference amplitude.

Chapter 6

Experimental Result

We used a 700MHz (a $\sim$16.4T magnet) Bruker NMR machine for this experiment. This chapter presents the experimental results.
Experiment Date: July 16 - July 18 2015

6.1 Thermal to PPS

The RF-selected thermal and the labelled-PPS states, the states after (d) and (e) of the state preparation step (Figure 5.2) respectively, were read-out by rotating C_7 by $\pi/2$ around y-axis. The RF-selected thermal state produced the 64 peaks in the C_7 spectrum as expected (Section 4.1.3), whereas the labelled-PPS state produced the expected singly peaked spectrum at the peak frequency corresponding to $|000000\rangle\langle 000000| X_{C_7}$ coherence (Z_{C_7} was rotated to X_{C_7} by the read-out pulse). Figure 6.2 shows the two spectra, clearly showing the single peak from the labelled-PPS spectrum (shown in red).

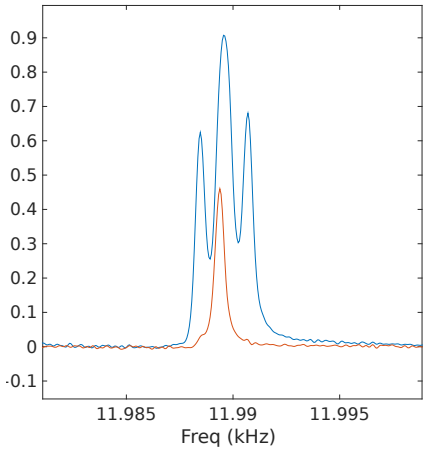

Figure 6.1: The zoomed-in figure of Figure 6.2 to show the frequency range integrated to produce Table 6.1

To quantify the goodness of the labelled PPS state, we compared the integral of peaks of the labelled

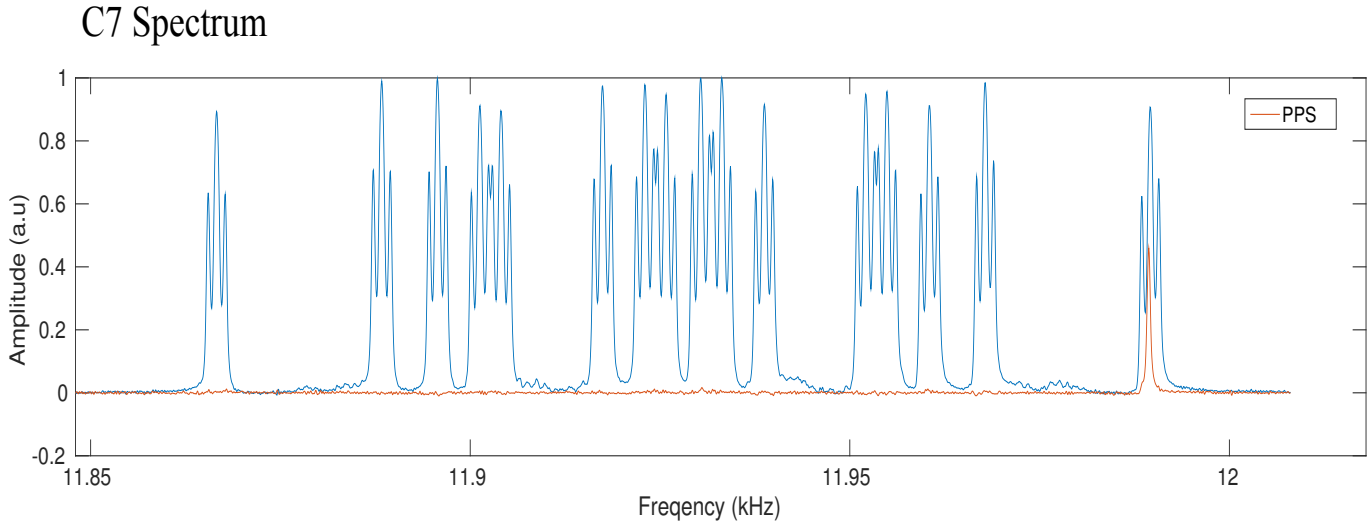

Figure 6.2: The C_7 spectra of the rf-selected thermal state and the labelled PPS state [the states after (d) and (e) of the state preparation step (Figure 5.2) observed with the C_7-$\pi/2$ rotation pulse, respectively] are shown in blue and red, respectively. The rf-selected thermal state produces 64 peaks as expected, and also the labelled PPS peak produces a single peak at the expected peak position. The spectra are normalized by the highest signal of the RF-selected thermal spectra

PPS and the RF-selected thermal state. In theory, there are four Lorentzian peaks with equal integral values at the right-most frequency range of the C_7 thermal spectrum (Figure 6.1), and one of the peaks indicates the signal from $|000000\rangle\langle 000000| X_{C_7}$. Therefore, in theory, the integral under the PPS peak should be a quarter of the integral under the four right most peaks of the thermal. We integrated by simply summing over the spectral data points. Figure 6.1 shows the range of spectra that were integrated. Table 6.1 shows that we get 73.8% of the theoretical signal.

Theory	Experiment	Exp/Theory
0.25	0.184±0.001	0.738±0.001

Table 6.1: RF-selected thermal and labelled-PPS Peak Ratio: The four right most peaks of the rf-selected thermal and labelled-PPS spectra were integrated to evaluate the goodness of the labelled-PPS state. The integral of thermal and the labelled PPS are normalized to integral of the thermal spectrum.

6.2 PPS to GD

If the pure state $|0000000\rangle\langle 0000000|$ is prepared as an initial state, the stabilizer operators (S_{pps}) of the state are Z_1, Z_2, Z_3, Z_4, Z_5, Z_6, and Z_7. Although I will not show a derivation here, these operators reconstruct the stabilizer operators of the ground state[1], when they evolve under the theoretical circuit which prepares the ground state (shown in Figure 3.2).

However, since our circuit starts from $|000000\rangle\langle 000000| Z_{C_7}$, the S_{pps} are modified to $Z_{C_1}Z_{C_7}$, $Z_{C_2}Z_{C_7}$, $Z_{C_3}Z_{C_7}$, $Z_{C_4}Z_{C_7}$, $Z_{C_5}Z_{C_7}$ and $Z_{C_6}Z_{C_7}$. The expectation values of these operators are +1: $\text{Tr}(\widetilde{\rho}_{\text{pps}}S^i_{\text{pps}})$ =1, where S^i_{pps} is one of the modified stabilizer operators (Figure 6.3). These operators transform to the following operators under the implemented ground state gate which is shown in Figure 5.3 (a):

$$
\begin{aligned}
&1. && Z_{C_4}Z_{C_7} \xrightarrow{U_{\text{ground}}} && Z_{C_2}Z_{C_4}Z_{C_7}\\
&2. && Z_{C_6}Z_{C_7} \xrightarrow{U_{\text{ground}}} && -Y_{C_4}X_{C_5}Y_{C_6}X_{C_7}\\
&3. && Z_{C_5}Z_{C_7} \xrightarrow{U_{\text{ground}}} && -Y_{C_4}Y_{C_5}X_{C_6}X_{C_7}\\
&4. && Z_{C_1}Z_{C_7} \xrightarrow{U_{\text{ground}}} && -Z_{C_1}Y_{C_4}X_{C_5}X_{C_6}Y_{C_7}\\
&5. && Z_{C_3}Z_{C_7} \xrightarrow{U_{\text{ground}}} && -Z_{C_3}Y_{C_4}X_{C_5}X_{C_6}Y_{C_7}\\
&6. && Z_{C_2}Z_{C_7} \xrightarrow{U_{\text{ground}}} && -X_{C_1}Y_{C_2}X_{C_3}Y_{C_4}X_{C_5}X_{C_6}Z_{C_7}
\end{aligned}
$$

Therefore, the ground state prepared experimentally should have +1 expectation values of the above transformed operators S_{ground} (Figure 6.3). We measured the expectation values of S_{pps} of the experimentally prepared labelled PPS state and also measured the expectation values of S_{ground} of the experimentally prepared ground state. For the S_{pps} measurements, a single read-out pulse which rotates C_7 by $\pi/2$ around y-axis is sufficient to measure all six operators; whereas five different read-out pulses are required (thus, five different measurements) to measure the S_{ground} operators. The read-out pulses are composed of the single qubit rotations that transform the product operator components of a density matrix corresponding to the S_{ground} operators to the measurable product operators in C_7 spectra, which are a combination of X_{C_7} or Y_{C_7} and Z_{C_i}s, where i indicates i^{th} C. For instance, the read-out pulse required to measure the expectation value of the second (#2 in the above list) S_{ground} operator is $X(\pi/2)_{C_4}Y(-\pi/2)_{C_5}X(\pi/2)_{C_6}$ (Table 5.1) which rotates $Y_{C_4}X_{C_5}Y_{C_6}X_{C_7}$ to $Z_{C_4}Z_{C_5}Z_{C_6}X_{C_7}$, which produces observable peaks

[1] Recall that this is the ground state of of the 7-qubit Kitaev's Lattice Model, a NMR Hamiltonian.

at C_7 spectrum. The experimentally measured expectation values are shown in Figure 6.4.

Figure 6.5 shows the experimental and simulated spectra of C_7 after the ground state preparation which were read out by the five different readout pulses. These spectra were used to estimate the S_{ground} operators.

Note on Error Analysis

Propagation of error: $f(\alpha, \beta),\ df = \sqrt{\frac{\partial f}{\partial \alpha}^2 d\alpha^2 + \frac{\partial f}{\partial \beta}^2 d\beta^2}$.

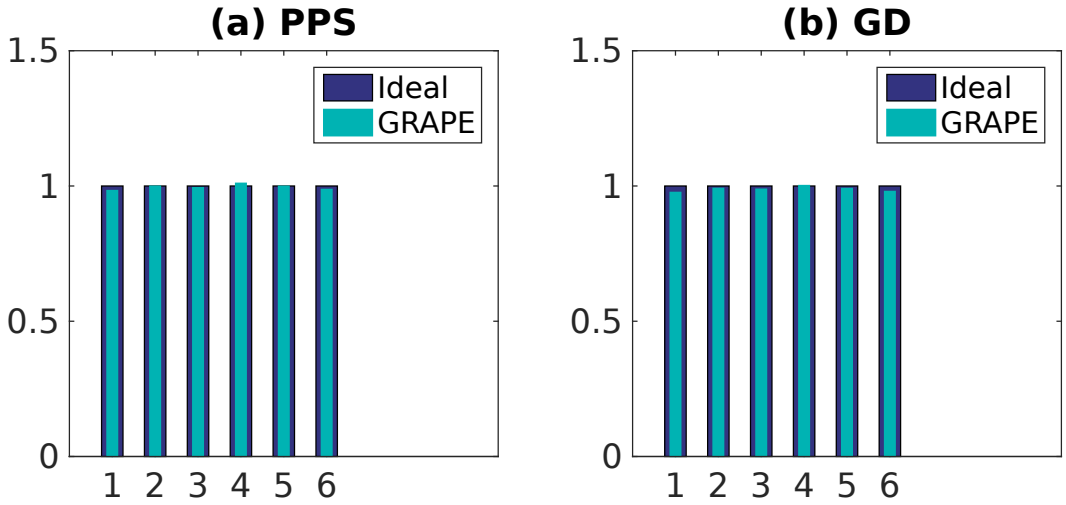

Figure 6.3: Expectation values of S_{pps} and S_{ground}: (a) the expectation values of S_{pps} of the theoretical and GRAPE labelled PPS state. The GRAPE labelled PPS state denotes the state numerically simulated using the GRAPE encoding,phase-cycling, and decoding pulses. Similarly, (b) shows the expectation values of S_{ground} of the theoretical and GRAPE ground states. The labelling of 1 to 6 measurements correspond to the stabilizer operators enumerated in the text above.

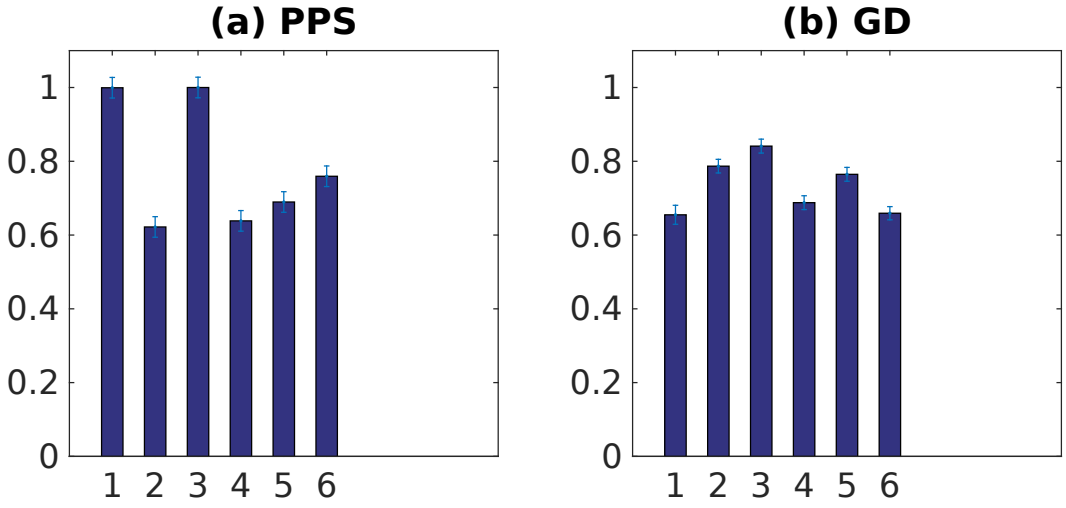

Figure 6.4: Expectation values of S_{pps} (a) and S_{ground} (b) of the experimental labelled PPS and ground state, respectively. These values were measured by applying five different read-out pulses, and the five different spectra produced from the different read-out pulses which are shown in Figure 6.5 were fitted using the least square method to estimate the coefficients of the peaks, and the expectation value of the desired operator were evaluated by taking the appropriate linear combinations of the estimated coefficients (Section 4.1.3). The standard deviations were calculated by using the method of the error propagation (refer to the 'Note on Error Analysis') with standard deviations of the fitting produced from estimation of the peak coefficients.

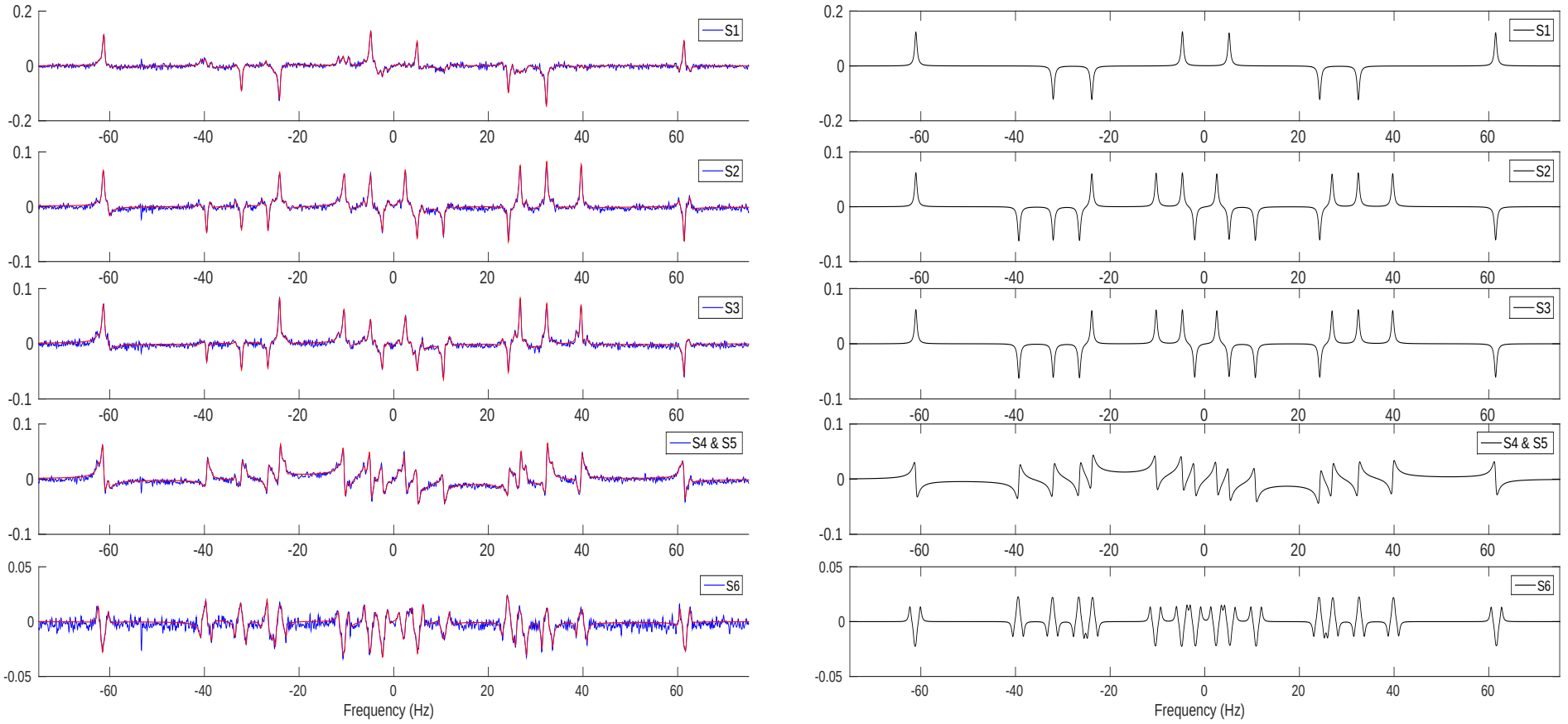

(a) (b)

Figure 6.5: NMR Spectra used to estimate the expectation values for the stabilizer operators: (a) experimental spectra (blue) and the fit (red) which was achieved by least squares fitting method. The legend shows which stabilizer(s) operator was(were) estimated for each spectra. (b) Theoretical spectra which were numerically simulated. Comparing (a) and (b) reflects that experiment and theory agrees well qualitatively. The number of scans collected for each spectrum are 70, 210, 210, 210, and 210 from the top to bottom figures, respectively.

6.3 PPS to Braiding

We measured the anyonic phases of the four different cases (refer to Figure 5.3, 5.4, and 5.1 to recall the abbreviations of GD, BDi, and MM):

1. **No braiding**: PPS $\rightarrow$ GD $\rightarrow$ MM $\rightarrow$ Read-out C_7
2. **Trivial braiding**: PPS $\rightarrow$ GD $\rightarrow$ BD0 $\rightarrow$ MM $\rightarrow$ Read-out C_7
3. **Non trivial braiding 1:** PPS $\rightarrow$ GD $\rightarrow$ BD1 $\rightarrow$ MM $\rightarrow$ Read-out C_7
4. **Non trivial braiding 2:** PPS $\rightarrow$ GD $\rightarrow$ BD2 $\rightarrow$ MM $\rightarrow$ Read-out C_7

Figure 6.6 shows the C_7 spectra of the four cases and the labelled PPS spectrum. The experimental spectra agree qualitatively with our theoretical predictions:

- In theory, we expect to get the same spectra for trivial and no braiding cases (noBD and BD0) and the same spectra for the two non-trivial braiding cases (BD1 and BD2). Figure 6.6 shows that the spectra of noBD and BD0 match well, and also BD1 and BD2 match well.
- In theory, we expect four peaks with the equal amplitude of a quarter of the labelled-PPS peak with for the four spectra. Although the simulated spectra are not shown in the figure, our experimental spectra match well with the simulated spectra.

6.3.1 Estimation of the Anyonic Phases

Recall that the state after the MM pulse is (Equation 5.2):

$$\widetilde{\rho}_{e\_exp} = \frac{1}{2}\left(|\psi_{mm}\rangle\langle\psi_{mm}| - \left|\psi'_{mm}\right\rangle\left\langle\psi'_{mm}\right| \right) \tag{6.1}$$

$$= \frac{1}{2}\left(|\alpha|^2 |\psi_{p0}\rangle\langle\psi_{p0}| + \alpha\beta^* |\psi_{p0}\rangle\langle\psi_{p1}| + \alpha^*\beta |\psi_{p1}\rangle\langle\psi_{p0}| + |\beta|^2 |\psi_{p1}\rangle\langle\psi_{p1}| - \left|\psi'_{mm}\right\rangle\left\langle\psi'_{mm}\right| \right), \tag{6.2}$$

where $|\psi_{mm}\rangle = \alpha|\psi_{p0}\rangle + \beta|\psi_{p1}\rangle$ with $|\psi_{p0}\rangle = |0000000\rangle + |0001111\rangle$ and $|\psi_{p1}\rangle = |1000000\rangle + |1001111\rangle$. The populations of $|\psi_{p0}\rangle\langle\psi_{p0}|$ and $|\psi_{p1}\rangle\langle\psi_{p01}|$ produce the NMR peaks at the four distinct frequencies centred around ω_{C_7} listed below: $|\psi_{p0}\rangle = |0000000\rangle + |0001111\rangle$ and $|\psi_{p1}\rangle =$

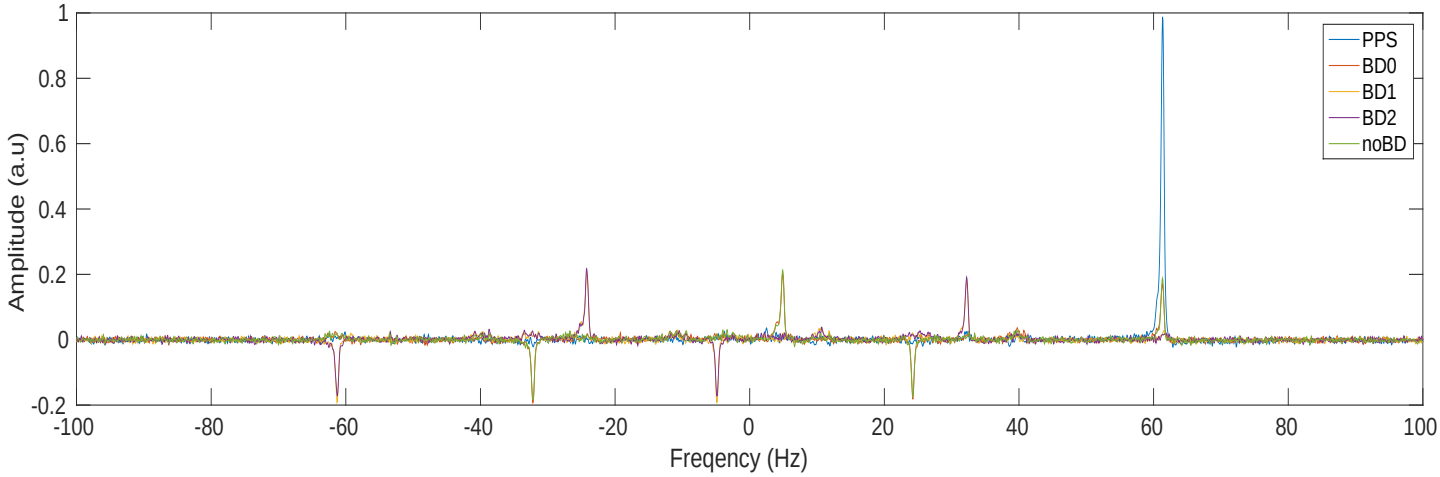

Figure 6.6: The C_7 spectra of the labelled PPS (PPS), trivial braiding (BD0), non-trivial braiding 1 (BD1), non-trivial braiding 2 (BD2), and no braiding (noBD). The spectra of BD0 and noBD are on the top of each other, which makes it hard to distinguish the two, similarly, BD1 and BD2 are on the top of each other. The spectra is normalized to the highest value of the labelled PPS spectra, and the frequency is centered around ω_{C_7}. The 70 scans were collected to produce the above spectra.

$|1000000\rangle + |1001111\rangle$. The populations of $|\psi_{p0}\rangle\langle\psi_{p0}|$ and $|\psi_{p1}\rangle\langle\psi_{p01}|$ produce the NMR peaks at the four distinct frequencies[2] centred around ω_{C_7} listed below up to a constant of a real number:

a. $|0000000\rangle\langle 0000000| \xrightarrow{R_y(\pi/2)_{C_7}} |0001000\rangle\langle 0001000| + \ldots$: 61.25Hz

b. $|0001111\rangle\langle 0001111| \xrightarrow{R_y(\pi/2)_{C_7}} |0000111\rangle\langle 0001111| + \ldots$: 24.09Hz

c. $|1000000\rangle\langle 1000000| \xrightarrow{R_y(\pi/2)_{C_7}} |1000000\rangle\langle 1001000| + \ldots$: 32.24Hz

d. $|1001111\rangle\langle 1001111| \xrightarrow{R_y(\pi/2)_{C_7}} |1000111\rangle\langle 1001111| + \ldots$: -4.93Hz

The top transitions a, b reflect $|\alpha|^2$, and the bottom two transitions c, d reflect $|\beta|^2$. As $\theta_{\text{anyon}} = 2\arctan(\sqrt{|\beta|^2/|\alpha|^2})$, theoretically, we expect no peaks at c and d for noBD and BD, resulting in $\theta_{\text{anyon}} = 0$, and we expect no peaks at a and b for BD1 and BD2, resulting in $\theta_{\text{anyon}} = \pi$. The spectra shown in Figure 6.7 qualitatively illustrate the expected behaviours. It should be noted that the four large peaks located other than a, b, c, d in the spectra shown in

[2]Recall that the 4-th qubit is C_7 (Figure 3.3).

Figure 6.7 result from $\left|\psi'_{\text{ground}}\right\rangle$ that we neglected from the analysis (Section 5.1.2).

We estimated $|\alpha|^2$ and $|\beta|^2$ by evaluating the real part[3] of the peak coefficients at the frequencies of a and b, and frequencies c and d, respectively (Figure 6.7). The coefficients of peaks at a and b were averaged to estimate $|\alpha|^2$, and similarly, the peaks at c and d were averaged to estimate $|\beta|^2$. To evaluate the coefficients we fitted the spectra with the Lorentzian function of the 64 peaks (Section 4.1.3) using the least-square method. The experimental results of $|\alpha|^2$, $|\beta|^2$ and θ_{anyon} are shown in Table 6.2 for each noBD, BD0, BD1 and BD2 case.

	$\|\alpha\|^2$		$\|\beta\|^2$		θ_{anyon}	
	Theory	EXP	Theory	EXP	Theory	EXP
No BD	1	0.83±0.01	0	0.01±0.01	0	(12.1±9.5)°
BD0	1	0.83±0.01	0	0.02±0.01	0	(17.4±6.0)°
BD1	0	0.05±0.01	1	0.85±0.01	π (180°)	(153.9±3.8)°
BD2	0	0.05±0.01	1	0.81±0.02	π (180°)	(151.4±3.8)°

Table 6.2: Experimentally evaluated $|\alpha|^2$, $|\beta|^2$ and θanyon values compared with the theoretical values: $|\alpha|^2$ and $|\beta|^2$ were evaluated by estimating the real parts of the peak coefficients at frequencies a, b, and c, d, respectively (Figure 6.7). The coefficients of peaks at a and b were averaged to estimate $|\alpha|^2$(a and b are ∼0.037 and ∼0.054, and ∼0.046 and ∼ 0.058 for BD1 and BD2, respectively), and similarly, the peaks at c and d were averaged to estimate $|\beta|^2$ (c and d are ∼0.81 and ∼0.89, and ∼0.89 and ∼ 0.72 for BD1 and BD2, respectively). Then, the anyonic phases were determined using the equation $\theta_{\text{anyon}} = 2\arctan\left(\sqrt{\frac{|\beta|^2}{|\alpha|^2}}\right)$. $|\alpha|^2$ and $|\beta|^2$ shown in the table are normalized to be in the range of $0 \leq |\alpha|^2$, $|\beta|^2 \leq 1$. The standard deviations δ of $|\alpha|^2$, $|\beta|^2$ are the fitting errors, and the standard deviations of θ_{anyon} were calculated from δ of $|\alpha|^2$, $|\beta|^2$ using the error propagation method.

[3]Since the populations are real numbers, and the NMR transition theoretically generates coherences up to a constant of a real number. Therefore, the only real coefficients were used to evaluate $|\alpha|^2$ and $|\beta|^2$. Theoretically, the imaginary part of the coefficients are zero. Therefore, any experimentally measured imaginary parts correspond to errors.

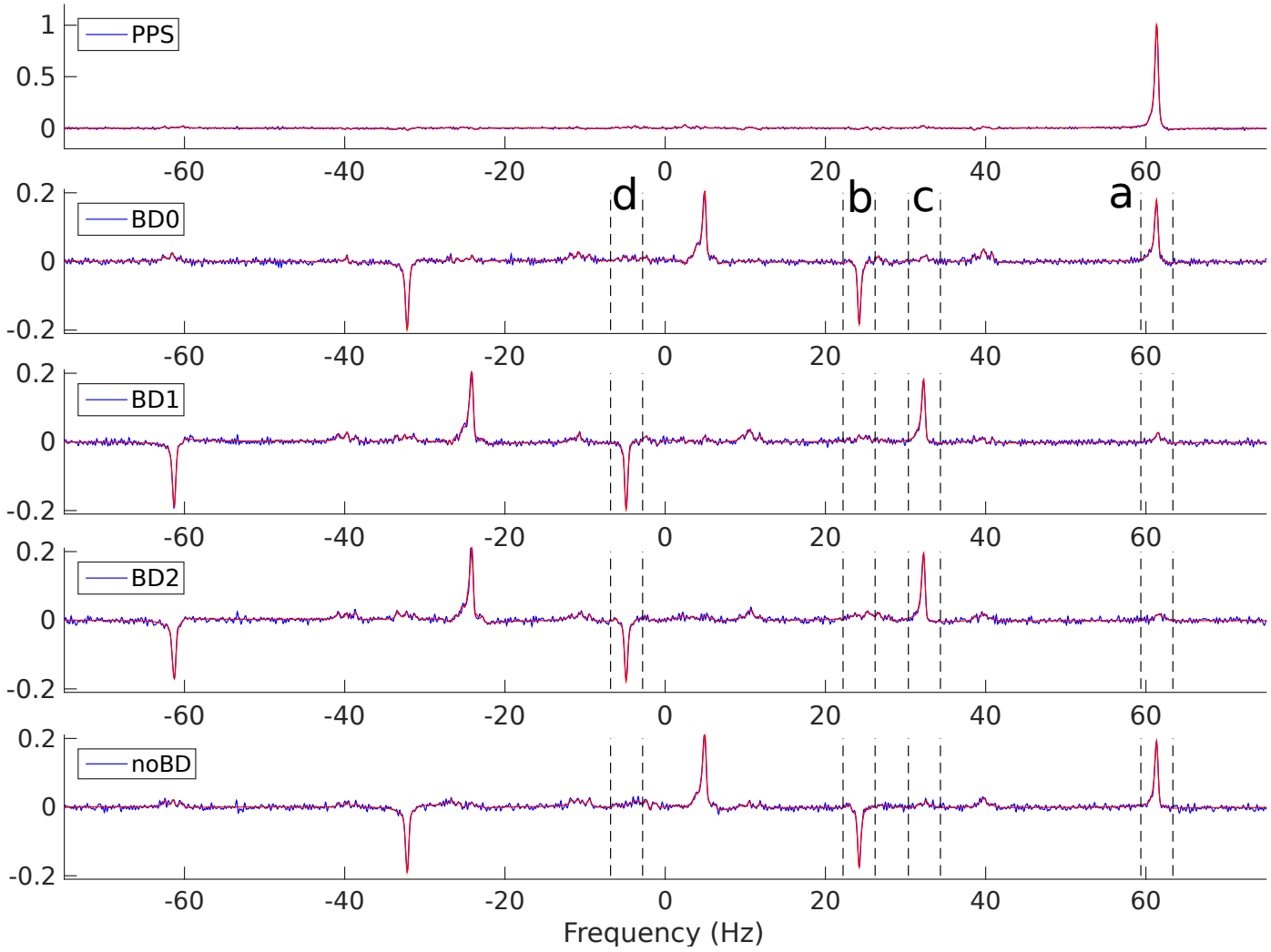

Figure 6.7: The C_7 NMR spectra after the PPS, BD0, BD1 and BD2 steps: the experimental data are shown in blue and the red spectra are the fit of the experimental spectra produced by the least square method.

Chapter 7

Discussion and Conclusion

The experimental results show that the anyonic phases under the two different non-trivial braiding paths agree within the errors, (153.93±3.82)° and (151.35±3.80)°. These experimental values clearly demonstrate the phase gained under the non-trivial paths compared to the cases of the trivial and no braiding paths [(17.37±6.03)° and (12.07±9.48)°, respectively]. However, the experimental anyonic phases do not agree with the theoretical values, which are 0° for the trivial and no braiding paths and 180° for the two non-trivial paths. This chapter discusses the sources of bias causing this deviation of the experimental phases from the theoretical phases.

7.1 Sensitivity of the Anyonic Phase Measurements

Recall that $\theta_{\text{anyon}} = 2\arctan(\sqrt{|\beta|^2/|\alpha|^2}\,)$ (Equation 3.8). We analyzed this function to examine how far the experimental phases are from the theoretical phases and to determine which of the parameters, $|\alpha|^2$and $|\beta|^2$, are crucial for evaluating the anyonic phase. Figure 7.1 (a) shows the experimental and theoretical phases, which appear as the red and black dots respectively, on the contour lines of the $\theta_{\text{anyon}}(|\alpha|^2, |\beta|^2)$ surface. This figure shows that for the cases of the two non-trivial braiding paths, the anyonic phase is sensitive to $|\alpha|^2$; whereas for the cases of trivial and no braiding operations, the anyonic phase is sensitive to $|\beta|^2$.

The gradient of the surface depicted as the blue arrows in Figure 7.1 (b) illustrates that θ_{anyon} changes rapidly as $|\beta|^2$ changes for the trivial and no braiding cases. The contour lines of the figure show that θ_{anyon} deviates almost to ∼29° (0.5 rad) when $|\alpha|^2 = 0.05$ ($0 \leq |\alpha|^2 \leq 1$). Figure 7.1 (c) shows the opposite behaviour for the two non-trivial braiding cases: θ_{anyon} is more sensitive to $|\alpha|^2$, deviating the anyonic phase from π to 0.9π [2.8rad (162°)] as $|\alpha|^2$ changes from 0 to 0.02.

Experimentally, we measured $|\alpha|^2$ $\sim$0.05 for both non-trivial braiding cases which result from integrals under the tiny peaks at a and c in Figure 6.7. Examining Figure 7.1 implies that to measure anyonic phases between 90% and 95% of the theoretical value (162 - 172°), we should experimentally measure $0.007 \leq |\alpha|^2 \leq 0.02$.

The uncertainties of the anyonic phases are larger for the trivial and no braiding cases ($\sim$10°) than the non-trivial braiding cases ($\sim$4°). This is because the surface near $\theta_{\text{anyon}} = 0$ is steeper than near $\theta_{\text{anyon}} = \pi$, which is evident from the gradient plot shown in Figure 7.1 (c). The lengths of the blue arrows in the figure are scaled to reflect the magnitude of the gradient.

7.2 Biases in $|\alpha|^2$ and $|\beta|^2$ Estimation

There are two main problems with how we estimate $|\alpha|^2$ and $|\beta|^2$:

1. In theory, $|\alpha|^2$ and $|\beta|^2$ can be determined through both the projective measurements on the spaces of $|\psi_{\text{p0}}\rangle$ and $|\psi_{\text{p1}}\rangle$ (Equation 5.2), or through the population measurements (Section 3.2). However erroneous states present due to gate imperfections or decoherence can contribute to the population measurements, causing bias in the estimation of $|\alpha|^2$ and $|\beta|^2$; whereas the projective measurements will still accurately measure $|\alpha|^2$ and $|\beta|^2$ originating from the states $|\psi_{\text{p0}}\rangle$ and $|\psi_{\text{p1}}\rangle$, respectively. Since we performed the population measurements, our experimental estimation of $|\alpha|^2$ and $|\beta|^2$ has biases from such sources.

2. To evaluate $|\alpha|^2$ and $|\beta|^2$, we estimated the relevant populations. Since in NMR, we cannot directly measure the populations, we estimated the relevant populations by inducing the transitions of the population to the single coherences. These induced single coherences were detected as the peaks at a, b, c, d in the C_7 NMR spectra, shown in Figure 6.7. The frequencies of a, b, c, d are listed in Section 5.1.5. However, there are four other populations which contribute to the peaks at the frequencies of a, b, c, d:

   1. $|0001000\rangle\langle 0001000| \xrightarrow{R_y(\pi/2)_{C_7}} |0001000\rangle\langle 0001000| + \ldots$: 61.25kHz
   2. $|0000111\rangle\langle 0000111| \xrightarrow{R_y(\pi/2)_{C_7}} |0000111\rangle\langle 0001111| + \ldots$: 24.09kHz
   3. $|1001000\rangle\langle 1001000| \xrightarrow{R_y(\pi/2)_{C_7}} |1000000\rangle\langle 1001000| + \ldots$: 32.24kHz
   4. $|1000111\rangle\langle 1000111| \xrightarrow{R_y(\pi/2)_{C_7}} |1000111\rangle\langle 1001111| + \ldots$: -4.93kHz

We expect that our estimated $|\alpha|^2$ and $|\beta|^2$ have such bias.

To examine how the above two problems affect the anyonic phase measurements, we numerically simulated the circuit starting from the ideal labelled PPS state using GRAPE pulses in presence of the decoherence effect. Then, we evaluated the anyonic phase with three different methods: the projective measurement (PRM), population measurement (PPM), and single coherence measurement (SCM). The SCM applies the ideal read-out pulse to measure single-coherences, mimicking the experimental measurement procedure.

For the simulation of the decoherence effect, we used the following assumptions:

- The environment is Markovian.
- The system and the environment are uncorrelated at t=0.
- We only considered the effect of dephasing due to T_2 effect and neglect the effect of amplitude damping, since T_1 is much larger than the circuit time.
- The dephasing noise is independent (or uncorrelated) between the qubits. The probability of an error happening on a given qubit does not affect the probability of an error happening on other qubits.
- When solving the master equation, we assumed that the dissipator D and the total Hamiltonian H_{tot} commute. Therefore, the evolution of of the state was simulated in a sequence of two steps: evolution by $e^{-iH_{\text{tot}}\Delta t}$ and subsequently, dephasing forΔt, where Δt was chosen to match the pulse discretization. The dephasing channel implements exponential decay of off-diagonal elements according to relevant linear combinations of carbon spins' T2 values.

	$\|\alpha\|^2$				$\|\beta\|^2$				θ_{anyon}			
	Theory	PRM	PPM	SCM	Theory	PRM	PPM	SCM	Theory	PRM	PPM	SCM
No BD	1	0.6622	0.7156	0.702	0	0.0176	0.0242	0.0172	0	0.3223 (18.47°)	0.3631 (20.20°)	0.3121 (17.88°)
BD0	1	0.6566	0.7096	0.6964	0	0.0176	0.0244	0.020	0	0.3247 (18.60°)	0.3669 (21.01°)	0.3342 (19.15°)
BD1	0	0.018	0.0248	0.0188	1	0.6542	0.7074	0.6948	π	2.8136 (161.21°)	2.7714 (158.79°)	2.8164 (161.37°)
BD2	0	0.0176	0.0242	0.0176	1	0.6546	0.7068	0.6928	π	2.8162 (161.36°)	2.7750 (158.00°)	2.8253 (161.88°)

Table 7.1: Numerical Simulation of the circuit with different types of measurement. $|\alpha|^2$ and $|\beta|^2$ shown in the table are normalized to be in the range of $0 \leq |\alpha|^2, |\beta|^2 \leq 1$.

The simulation results shown in Table 7.1 demonstrate that different measurement methods result in $\sim 3^\circ$ differences in the anyonic phases. This small difference, which is comparable

to the standard deviation of the experimental anyonic phases, ensures that the SCM method is still a reliable way to estimate the anyonic phase. Moreover, we checked through the simulation that the SCM produces the same phases as the PPM if we let the four other populations which contribute to the phase be zero before applying the read out pulse (see #2 in above list).

However, even the PRM results in an anyonic phase that is different from the theoretical values. These are due to gate imperfections of the GRAPE pulses and also the decoherence effect. These are discussed in the subsequent sections.

7.3 Effect of Gate Imperfections on the Anyonic Phase Estimation

Even if $|\alpha|^2$ and $|\beta|^2$ can be accurately estimated, $\theta_{\text{anyon}} = 2\text{arctan}(\sqrt{|\beta|^2/|\alpha|^2}\ )$ no longer accurately determines the anyonic phase in presence of gate imperfections. Numerically simulating the circuit with the GRAPE pulses in absence of decoherence results in anyonic phases of $\sim$175° for the non-trivial braiding operations using the PPM. Therefore, to estimate the anyonic phase independent of the initial state imperfections and imperfections of the measurement gate [MM gate in Figure 5.3 (b)], a different equation than $\theta_{\text{anyon}} = 2\text{arctan}(\sqrt{|\beta|^2/|\alpha|^2}\ )$ is required. However, it is difficult to find such an equation that is accurate and can be implemented. Since the braiding operation is 1ms, whereas the ground state and measurement pulses are 60ms, we expect that the ground state and measurement (MM) pulse imperfections contribute more than braiding to imperfections in phase estimation.

As an example, we analyzed how imperfections in the ground state lead to a bias. For simplicity, we considered the circuit starting with the pure state $|0000000\rangle$, although we started with the mixed state $|000000\rangle\langle 000000| Z_{C_7}$ in experiments. The imperfect ground state $|\Phi_{\text{ground}}\rangle$ can be expressed as:

$$|\Phi_{\text{ground}}\rangle = \alpha' |\psi_{\text{ground}}\rangle + \beta' |\psi_{\text{excited}}\rangle + \gamma' |\psi_{\text{error}}\rangle \tag{7.1}$$

where $|\psi_{\text{excited}}\rangle = Z_1 |\psi_{\text{ground}}\rangle$, $|\psi_{\text{error}}\rangle$ are the states resulting from gate imperfections, and $|\psi_{\text{ground}}\rangle$, $|\psi_{\text{excited}}\rangle$ and $|\psi_{\text{error}}\rangle$ are orthogonal to each other. We specifically considered $|\psi_{\text{excited}}\rangle$ separate from $|\psi_{\text{error}}\rangle$, since this excited state contributes to the measurements of $|\alpha|^2$ and $|\beta|^2$. To see how $|\Phi_{\text{ground}}\rangle$ evolves under the perfect braiding (BD) and measurement (MM) operations, we look at three possibilities:

1. Ideal Case:

$$|\psi_{\text{ground}}\rangle \xrightarrow{\text{BD or no BD + MM}} \alpha\,|\psi_{\text{p0}}\rangle + \beta\,|\psi_{\text{p1}}\rangle \tag{7.2}$$

2. Imperfect Ground State with no braiding operations:

$$\alpha'\,|\psi_{\text{ground}}\rangle + \beta'\,|\psi_{\text{excited}}\rangle + \gamma'\,|\psi_{\text{error}}\rangle \xrightarrow{\text{no BD + MM}} \alpha'\,|\psi_{\text{p0}}\rangle + \beta'\,|\psi_{\text{p1}}\rangle + \gamma'\,|\phi_{\text{error}}\rangle \tag{7.3}$$

3. Imperfect Ground State with braiding operations:

$$\alpha'\,|\psi_{\text{ground}}\rangle + \beta'\,|\psi_{\text{excited}}\rangle + \gamma'\,|\psi_{\text{error}}\rangle \xrightarrow{\text{BD + MM}} \widetilde{\alpha}\,|\psi_{\text{p0}}\rangle + \widetilde{\beta}\,|\psi_{\text{p1}}\rangle + \widetilde{\gamma}\,|\phi_{\text{error}}\rangle \tag{7.4}$$

With careful calculations, one can show that $\widetilde{\alpha} \neq \alpha$ and $\widetilde{\beta} \neq \beta$. Instead, $\widetilde{\alpha}$ and $\widetilde{\beta}$ depend on θ_{anyon}, α', and β':

$$\widetilde{\alpha} = -\alpha'\sin(\eta) - \beta'\cos(\eta) \tag{7.5}$$

$$\widetilde{\beta} = -\alpha'\cos(\eta) - \beta'\sin(\eta) \tag{7.6}$$

where $\eta = (\theta_{\text{anyon}} - \pi)/2$. Therefore, the anyonic phase cannot be calculated by taking the ratio of $|\widetilde{\alpha}|^2$ and $|\widetilde{\beta}|^2$, since $\theta_{\text{anyon}} \neq 2\arctan\left(\sqrt{|\widetilde{\beta}|^2/|\widetilde{\alpha}|^2}\right)$. Instead, the following equation is derived:

$$\left|\frac{\widetilde{\alpha}}{\widetilde{\beta}}\right|^2 = \frac{\left|\frac{\alpha'}{\beta'}\right|^2\tan^2(\eta) + 2\left|\frac{\alpha'}{\beta'}\right|\tan(\eta)\cos(\phi_{\alpha'} - \phi_{\beta'}) + 1}{\left|\frac{\alpha'}{\beta'}\right|^2 - 2\left|\frac{\alpha'}{\beta'}\right|\tan(\eta)\cos(\phi_{\alpha'} - \phi_{\beta'}) + \tan^2(\eta)}, \tag{7.7}$$

where ϕ_i is the phase of the coefficient i. Since the assumption that both braiding and measurement gates are error-free is not true for our the experimental situation. Since the pulse complexities of the ground state preparation and measurement pulses are similar, we expect similar degrees of errors for both operations. Therefore, we cannot use Equation 7.7 to estimate the anyonic phase. Even the numerical simulation of the circuit using the GRAPE pulses shows that Equation 7.7 fails when the ideal measurement pulse is replaced with the GRAPE pulse [1].

[1] In principle, one can come up with a different experimental proposal which does not use the measurement pulse (no basis transformation), and measure the phase directly after the braiding with the appropriate readout pulses. In such case, one could use Equation 7.7.

7.4 Effect of Dephasing on the Anyonic Phase Estimation

If we include the dephasing effect on the top of GRAPE pulse imperfections in the numerical simulation, the non-trivial anyonic phases drop to 161°(Table 7.1) from 175° for the PPM. To understand how dephasing affects the anyonic phase, we studied a single-qubit example similar to our experimental scheme which is shown below.

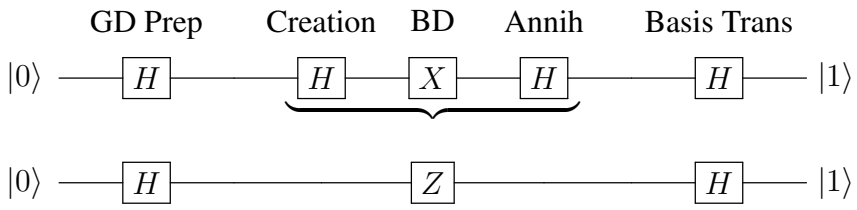

In the above circuit, 'Gd Prep', 'Creation', 'BD', 'Annih', and 'Basis Trans' indicate the ground state preparation step, creation of superposition state, braiding, annihilation step, and transformation of basis steps. As in our experiments, 'Creation', 'BD' and 'Annih' steps are compressed into a single step of a phase flip operation. The state after each step is written below:

$$|0\rangle \xrightarrow{\text{ground state prep}} \frac{|0\rangle + |1\rangle}{\sqrt{2}} \tag{7.8}$$

$$\xrightarrow{\text{anyon creation + braiding + annihilation}} \frac{|0\rangle + e^{i\theta}|1\rangle}{\sqrt{2}} \tag{7.9}$$

$$\xrightarrow{\text{change of basis}} \frac{(1+e^{i\theta})|0\rangle + (1-e^{i\theta})|1\rangle}{2}, \qquad \theta = 2\arctan\left(\frac{1-e^{i\theta}}{1+e^{i\theta}}\right) \tag{7.10}$$

Instead of the ground state preparation giving $(|0\rangle + |1\rangle)/\sqrt{2}$, we analyzed the case where the dephasing effect changes the pure state to a mixed state:

$$\rho = \frac{1}{\sqrt{2}}\begin{bmatrix}1 & 1\\ 1 & 1\end{bmatrix} \xrightarrow{\text{dephasing}} \frac{1}{\sqrt{2}}\begin{bmatrix}1 & \lambda\\ \lambda & 1\end{bmatrix}, \quad \lambda < 1 \tag{7.11}$$

For such a case, the θ estimation acquires the bias from the dephasing effect:

$$\theta = 2\arctan\left(\sqrt{\frac{1+\lambda}{1-\lambda}}\right) \tag{7.12}$$

Of course for the accurate picture, one needs to solve for master equation considering the dephasing effect during the gate; however, the above analysis provides a rough picture of how dephasing would affect anyonic phase.

7.5 Conclusions

Following from our experimental result and analysis, we answered the questions introduced in Chapter 1:

- Are the braiding operations in the 7-qubit model resilient to decoherence of our experimental system?

  - No, both decoherence and gate imperfections deviated the experimental anyonic phases from the theoretical value of 180° to $(153.9 \pm 3.8)^\circ$ and $(151.4 \pm 3.8)^\circ$ for the non-trivial paths l_1 and l_2, respectively. However, we expect that the contributions of decoherence and gate imperfections to the anyonic phases mostly resulted from the ground state preparation and basis transformation (MM pulse) steps, as these steps are significant longer (60ms each) than the actual braiding step (1ms). Moreover, it is difficult to distinguish the two effects and to determine how much the gate imperfections and decoherence independently deviated the phases.

- Can we experimentally demonstrate the path independence property of anyonic braiding using NMR QIP?

  - Yes, the anyonic phases of the two non-trivial path, l_1 and l_2, agree within the errors: $(153.9 \pm 3.8)^\circ$ and $(151.4 \pm 3.8)^\circ$ for l_1 and l_2, respectively.

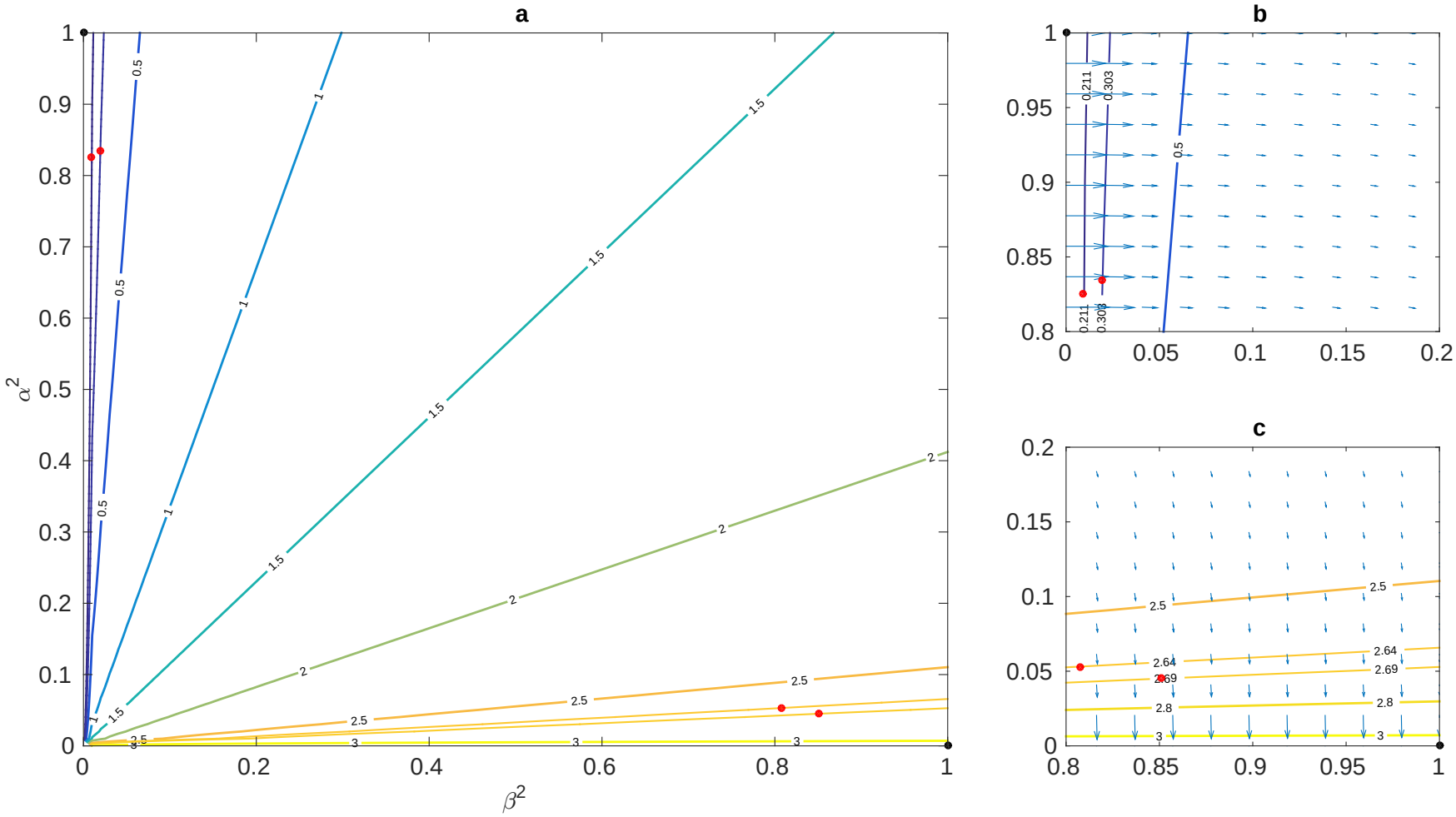

Figure 7.1: The contour lines of the anyonic phase function, $\theta_{\text{anyon}} = 2\arctan(\sqrt{|\beta|^2/|\alpha|^2})$ in radian: a) the figure showing the full ranges of $|\alpha|^2$ and $|\beta|^2$,$|\alpha|^2$ and $|\beta|^2$ are normalized such that 0 ¡ $|\alpha|^2$, $|\beta|^2$ ¡ 1. The red points correspond to experimental values of anyonic phases, the top left points are of trivial braiding and no-braiding operations; whereas the points at the bottom right corner are of two non-trivial braiding operations. The lines passing through the red points are the contour lines corresponding to the experimental values. The black points at the top left and bottom right vertices are theoretical values of α^2 and β^2 corresponding to trivial and non-trivial braiding operations, respectively. b) the areas where the anyonic phase is 0, which is the case for the trivial braiding and no braiding operations. The gradient of the surface is depicted as the blue arrows, which are scaled to reflect the magnitude. c) the areas where the anyonic phase is π, which is the case for the two non-trivial braiding operations. These figures indicate that for the cases of the two non-trivial braiding paths, the anyonic phase is sensitive to $|\alpha|^2$; whereas for the cases of trivial and no braiding operations, the anyonic phase is sensitive to $|\beta|^2$.

References

[1] Dorit Aharonov and Michael Ben-Or. Fault-Tolerant Quantum Computation with Constant Error Rate. *SIAM Journal on Computing*, 38(4):1207–1282, January 2008.

[2] W. A. Anderson and R. Freeman. Influence of a Second Radiofrequency Field on High Resolution Nuclear Magnetic Resonance Spectra. *The Journal of Chemical Physics*, 37(1):85–103, 1962.

[3] D. G. Cory, M. D. Price, W. Maas, E. Knill, R. Laflamme, W. H. Zurek, T. F. Havel, and S. S. Somaroo. Experimental Quantum Error Correction. *Physical Review Letters*, 81:2152–2155, 1998.

[4] Ben Criger, Gina Passante, Daniel Park, and Raymond Laflamme. Recent advances in nuclear magnetic resonance quantum information processing. *Philosophical transactions. Series A, Mathematical, physical, and engineering sciences*, 370(1976):4620–35, 2012.

[5] Guanru Feng, Guilu Long, and Raymond Laflamme. Experimental simulation of anyonic fractional statistics with an NMR quantum-information processor. *Physical Review A*, 88(2):022305, August 2013.

[6] Richard P. Feynman. Quantum mechanical computers. *Foundations of Physics*, 16(6):507–531, 1986.

[7] Evan M. Fortunato, Marco A. Pravia, Nicolas Boulant, Grum Teklemariam, Timothy F. Havel, and David G. Cory. Design of strongly modulating pulses to implement precise effective Hamiltonians for quantum information processing. *Journal of Chemical Physics*, 116(17):7599–7606, 2002.

[8] Austin G. Fowler, Matteo Mariantoni, John M. Martinis, and Andrew N. Cleland. Surface codes: Towards practical large-scale quantum computation. *Physical Review A - Atomic, Molecular, and Optical Physics*, 86(3), 2012.

[9] Peter Gans. *Data Fitting in the Chemical Sciences: By the Method of Least Squares*. Wiley, 1992.

[10] E. Hahn. Spin Echoes, 1950.

[11] Y. J. Han, R. Raussendorf, and L. M. Duan. Scheme for demonstration of fractional statistics of anyons in an exactly solvable model. *Physical Review Letters*, 98(15), 2007.

[12] YJ Han, R Raussendorf, and LM Duan. A scheme for demonstration of fractional statistics of anyons in an exactly solvable model. 0:5–8.

[13] Phillip Kaye, Raymond Laflamme, and Michele Mosca. An Introduction to Quantum Computing. January 2007.

[14] Navin Khaneja, Timo Reiss, Cindie Kehlet, Thomas Schulte-Herbrüggen, and Steffen J Glaser. Optimal control of coupled spin dynamics: design of NMR pulse sequences by gradient ascent algorithms. *Journal of magnetic resonance (San Diego, Calif. : 1997)*, 172(2):296–305, February 2005.

[15] A.Yu. Kitaev. Fault-tolerant quantum computation by anyons. *Annals of Physics*, 303(1):2–30, 2003.

[16] E Knill. Quantum computing with realistically noisy devices. *Nature*, 434:39–44, 2005.

[17] E. Knill, R. Laflamme, R. Martinez, and C. Negrevergne. Benchmarking quantum computers: The five-qubit error correcting code. *Physical Review Letters*, 86:5811–5814, 2001.

[18] E Knill, R. Laflamme, R Martinez, and C.-H. Tseng. An algorithmic benchmark for quantum information processing, 2000.

[19] Emanuel Knill, Raymond Laflamme, and WH Zurek. Resilient quantum computation. *Science*, 279(January), 1998.

[20] Raymond Laflamme, Cesar Miquel, Juan Pablo Paz, and Wojciech Hubert Zurek. Perfect Quantum Error Correcting Code, 1996.

[21] B. Lee, W. M. Witzel, and S. Das Sarma. Universal pulse sequence to minimize spin depahasing in the central spin decoherence problem. *Physical Review Letters*, 100(16), 2008.

[22] Malcolm H. Levitt. Composite pulses, 1986.

[23] Malcolm H. Levitt. *Spin Dynamics: Basics of Nuclear Magnetic Resonance*. Wiley, 2001.

[24] Chao Yang Lu, Wei Bo Gao, Otfried Gühne, Xiao Qi Zhou, Zeng Bing Chen, and Jian Wei Pan. Demonstrating anyonic fractional statistics with a six-qubit quantum simulator. *Physical Review Letters*, 102, 2009.

[25] Chetan Nayak, Steven H. Simon, Ady Stern, Michael Freedman, and Sankar Das Sarma. Non-Abelian anyons and topological quantum computation. *Reviews of Modern Physics*, 80(3):1083–1159, 2008.

[26] Michael A. Nielsen and Isaac L. Chuang. *Quantum Computation and Quantum Information*. Cambridge University Press, 2000.

[27] J. K. Pachos, W. Wieczorek, C. Schmid, N. Kiesel, R. Pohlner, and H. Weinfurter. Revealing anyonic features in a toric code quantum simulation. *New Journal of Physics*, 11, 2009.

[28] Jiannis K. Pachos. Video library: Jiannis Pachos, Topological quantum computation. Lecture 1.

[29] Jiannis K. Pachos. *Introduction to Topological Quantum Computation*. 2012.

[30] Teodor Parella. WALTZ SCHEME.

[31] Isidor Isaac Rabi, J. R. Zacharias, S. Millman, and P. Kusch. A New Method of Measuring Nuclear Magnetic Moment. *Physical Review*, 53(4):318, 1938.

[32] Hans J. Reich. 8.2 The Nuclear Overhauser Effect.

[33] Gordon S. Rule and T Kevin Hitchens. Fundamentals of Protein NMR Spectroscopy — Springer.

[34] Colm A. Ryan. Characterization and Control in Large Hilbert Spaces, 2008.

[35] Steve Simon. Steve Simon - Topological Quantum Computing (Part 1) - CSSQI 2012 - YouTube, 2012.

[36] Steve Simon. Steve Simon - Topological Quantum Computing (Part 2) - CSSQI 2012 - YouTube, 2012.

[37] Götz S. Uhrig. Keeping a quantum bit alive by optimized π-pulse sequences. *Physical Review Letters*, 98(10), 2007.

[38] Jeffrey Urbauer. Lecture on Double-Resonance Experiments.

[39] Zhenghan Wang. Topological quantum computation. *American Mathematical Soc.*, No. 112, 2010.

[40] Frank Wilczek. Quantum mechanics of fractional-spin particles. *Physical Review Letters*, 49(14):957–959, 1982.

[41] John Wolberg. *Data Analysis Using the Method of Least Squares: Extracting the Most Information from Experiments*. Springer Science & Business Media, 2006.

[42] Wen Yang and Ren Bao Liu. Universality of uhrig dynamical decoupling for suppressing qubit pure dephasing and relaxation. *Physical Review Letters*, 101(18), 2008.

[43] Jingfu Zhang, Dorian Gangloff, Osama Moussa, and Raymond Laflamme. Experimental quantum error correction with high fidelity, 2011.